AGU PUBLICATIONS

JGR

Journal of Geophysical Research: Atmospheres

RESEARCH ARTICLE
10.1002/2014JD022666

Key Points:
- Multilayer energy balance schemes for snow and glacier
- Estimating snowmelt, glaciermelt, and rainfall runoff contribution
- Basin-scale compulation of glacier mass balance

Correspondence to:
M. Shrestha,
maheswor@hydra.t.u-tokyo.ac.jp

Citation:
Shrestha, M., T. Koike, Y. Hirabayashi, Y. Xue, L. Wang, G. Rasul, and B. Ahmad (2015), Integrated simulation of snow and glacier melt in water and energy balance-based, distributed hydrological modeling framework at Hunza River Basin of Pakistan Karakoram region, *J. Geophys. Res. Atmos.*, *120*, 4889–4919, doi:10.1002/2014JD022666.

Received 2 OCT 2014
Accepted 29 APR 2015
Accepted article online 5 MAY 2015
Published online 29 MAY 2015

Integrated simulation of snow and glacier melt in water and energy balance-based, distributed hydrological modeling framework at Hunza River Basin of Pakistan Karakoram region

Maheswor Shrestha[1], Toshio Koike[1], Yukiko Hirabayashi[2], Yongkang Xue[3], Lei Wang[4], Ghulam Rasul[5], and Bashir Ahmad[6]

[1]Department of Civil Engineering, University of Tokyo, Tokyo, Japan, [2]Institute of Engineering Innovation, University of Tokyo, Tokyo, Japan, [3]Department of Geography, University of California, Los Angeles, California, USA, [4]Institute of Tibetan Plateau Research, Chinese Academy of Sciences, Beijing, China, [5]Pakistan Meteorological Department, Islamabad, Pakistan, [6]Pakistan Agriculture Research Council, Islamabad, Pakistan

Abstract Energy budget-based distributed modeling of snow and glacier melt runoff is essential in a hydrologic model to accurately describe hydrologic processes in cold regions and high-altitude catchments. We developed herein an integrated modeling system with an energy budget-based multilayer scheme for clean glaciers, a single-layer scheme for debris-covered glaciers, and multilayer scheme for seasonal snow over glacier, soil, and forest within a distributed biosphere hydrological modeling framework. Model capability is demonstrated for Hunza River Basin (13,733 km^2) in the Karakoram region of Pakistan on a 500 m grid for 3 hydrologic years (2002–2004). Discharge simulation results show good agreement with observations (Nash-Sutcliffe efficiency = 0.93). Flow composition analysis reveals that the runoff regime is strongly controlled by the snow and glacier melt runoff (50% snowmelt and 33% glacier melt). Pixel-by-pixel evaluation of the simulated spatial distribution of snow-covered area against Moderate Resolution Imaging Spectroradiometer-derived 8 day maximum snow cover extent data indicates that the areal extent of snow cover is reproduced well, with average accuracy 84% and average absolute bias 7%. The 3 year mean value of net mass balance (NMB) was estimated at +0.04 myr^{-1}. It is interesting that individual glaciers show similar characteristics of NMB over 3 years, suggesting that both topography and glacier hypsometry play key roles in glacier mass balance. This study provides a basis for potential application of such an integrated model to the entire Hindu-Kush-Karakoram-Himalaya region toward simulating snow and glacier hydrologic processes within a water and energy balance-based, distributed hydrological modeling framework.

1. Introduction

The Hindu-Kush-Karakoram-Himalaya (HKKH) region, often called "Water Towers of Asia," provides natural reserves of fresh water in the form of snow and glaciers that sustain water availability in mountainous or Himalayan areas, as well as on adjacent plains [*Viviroli et al.*, 2007; *Immerzeel et al.*, 2010]. It has been noted that snow cover dynamics in these high-elevation regions influences water availability in spring, at the onset of the growing season [*Barnett et al.*, 2005; *Lemke et al.*, 2007; *Viviroli et al.*, 2007; *Immerzeel et al.*, 2009; *Bookhagen and Burbank*, 2010]. The snow hydrology of these regions is expected to be more susceptible to climate change, because significant air temperature warming affects the seasonality of runoff [e.g., *Singh and Singh*, 2001; *Akhtar et al.*, 2008; *Immerzeel et al.*, 2010, 2013]. Moreover, the rate of glacier retreat in the Greater Himalaya region is reportedly rapidly increasing in recent decades, which is considered one of the consequences of global warming [*Ageta et al.*, 2001; *Dyurgerov and Meier*, 2004; *Lemke et al.*, 2007; *Cogley*, 2011; *Benn et al.*, 2012]. Nevertheless, many central Karakoram glaciers are reported advancing [*Hewitt*, 2005; *Bolch et al.*, 2012; *Gardelle et al.*, 2012, 2013; *Kääb et al.*, 2012].

Hydrometeorological observations and glacier mass balance studies in the HKKH region have been rare and often intermittent over recent decades, owing to the hostile climate and remote and rugged terrain. Despite this, it is worthwhile understanding via an integrated approach the variability of hydrologic processes, regarding their response not only to snow and glacierized areas but also to forested and other land use areas. It is a critical but daunting challenge for hydrologic models to accurately describe spatiotemporal

distributions of glacier mass balance and seasonal snow evolution (accumulation and ablation) across land, forest, and glaciated regions in different climates, from tropical to arctic so that snowmelt, glacier melt, and rainfall contributions to streamflow may be precisely addressed within an integrated approach. In addition, this will assist to understand how the basin topography affects the glacier melting and accumulation.

To this end, many diverse approaches have been taken in developing hydrologic models for better representation of snow and glacier processes within conceptual and distributed hydrologic modeling frameworks. Snow and glacier melt modules in hydrologic models vary from simplified temperature index models [e.g., *Braun et al.*, 1993; *Gurtz et al.*, 1999; *Schaefli et al.*, 2005; *Immerzeel et al.*, 2009; *Luo et al.*, 2013] to physically based energy balance models [e.g., *Klok and Oerlemans*, 2002; *Hock*, 2005; *Kotlarski et al.*, 2010; *Reid et al.*, 2012]. Temperature index melt modeling methods are common in estimation of both snow and glacier melt and are mainly used in conceptual hydrologic models [*Braun et al.*, 1993; *Rana et al.*, 1997; *Kayastha et al.*, 2005; *Schaefli et al.*, 2005; *Rees and Collins*, 2006; *Konz et al.*, 2007; *Immerzeel et al.*, 2009, 2010; *Bookhagen and Burbank*, 2010; *Luo et al.*, 2013]. Many attempts have been made to strengthen degree-day models by incorporating more variables, such as wind speed, vapor pressure, or radiation [e.g., *Cazorzi and Fontana*, 1996; *Hock*, 1999; *Li and Williams*, 2008]. However, these cannot accurately simulate complex situations [*Walter et al.*, 2005] such as rain-on-snow events or in very dry climates where temperature cannot be directly correlated to energy for snowpack melting. Conversely, energy balance models provide thorough descriptions of energy and mass exchange between snow/glacier surfaces and the atmosphere. The models do this by following their process-based physical rules, which help analyze more precisely the sensitivity to climate change of the hydrologic cycle in snow- and glacier-fed river basins. Given the complexities, many distributed hydrologic models (DHMs) use a hybrid approach, i.e., an energy balance scheme for estimation of snowmelt and a degree-day method for estimation of glacier melt. However, much research has been done in the development and application of energy balance-based, spatially distributed, glacier mass balance models, focusing on a few individual glaciers outside the framework of the distributed biosphere, hydrological modeling approach [*Hock*, 1999; *Brock et al.*, 2000; *Klok and Oerlemans*, 2002; *Machguth et al.*, 2006; *Anslow et al.*, 2008; *Sicart et al.*, 2011; *Zhang et al.*, 2011; *Reid et al.*, 2012]. These models are basically designed for estimation of glacier melt runoff and cannot express basin-scale hydrology under different land uses (such as a wide range of forest and bare land) within an integrated approach.

A few DHMs have included sophisticated, snow-soil-vegetation-atmosphere-transfer (SSVAT)-based, single-layer to multilayer energy balance snow schemes [*Storck and Lettenmaier*, 1999; *Soulis et al.*, 2000; *Wang et al.*, 2009a; *Shrestha et al.*, 2010] for better representation of integrated hydrologic processes of seasonal snow evolution at a basin scale, with different land use characteristics. *Storck and Lettenmaier* [1999] introduced a two-layer snowpack model into the Distributed Hydrology-Soil-Vegetation Model (DHSVM) [*Wigmosta et al.*, 1994], which was later introduced in the Variable Infiltration Capacity model (VIC model) [*Liang et al.*, 1994] by *Cherkauer et al.* [2003]. The WATCLASS model [*Soulis et al.*, 2000; *Fassnacht and Soulis*, 2002], developed by coupling the WATFLOOD [*Kouwen et al.*, 1993] hydrologic model with the CLASS [*Verseghy,* 1991, 2009] land surface model, has a simple, single-layer, energy balance snow scheme. *Wang et al.* [2009a] developed the Water and Energy Budget-based Distributed Hydrological Model (WEB-DHM) by coupling the Simple Biosphere model version 2 (SiB2) [*Sellers et al.*, 1996] land surface model and the Geomorphology-Based Hydrological Model [*Yang et al.*, 2004]. Snow physics in WEB-DHM was further improved by coupling the three-layer energy balance snow scheme of the Simplified Simple Biosphere 3 model (SSiB3) [*Xue et al.*, 2003] and the prognostic albedo scheme of the Biosphere-Atmosphere Transfer Scheme (BATS) [*Dickinson et al.*, 1993; *Yang et al.*, 1997]. A few recent studies have focused on incorporation of the glacier melt module in SSVAT coupled DHM to investigate the contribution of glacier melt in mountainous river basins where glacial coverage is significant (VIC model [*Schaner et al.*, 2012; *Zhao et al.*, 2013; *Zhang et al.*, 2013]; DHSVM model [*Naz et al.*, 2014]). However, many studies have centered on integration of a glacier melt module in conceptual hydrologic models. Realizing the lack of accurate representation of energy balance-based, snow and glacier processes in SSVAT-based DHMs, the present study focuses on enhancement of an SSVAT-based DHM, WEB-DHM-S (WEB-DHM with improved snow physics) [*Shrestha et al.,* 2010, 2012a, 2012b]. This is done by developing and integrating the energy balance-based, glacier melt module for debris-free clean glaciers and debris-covered glaciers in conjunction with multilayer snow processes to accurately simulate basin-scale hydrology in snow- and

Table 1. A Summarizing Table of Relevant Recent Studies on Snow and Glaciermelt Schemes in Basin-Scale Hydrologic Models[a]

Relevant Studies	Major Contribution	Limitation
Tahir et al. [2011b]	Efficient application of SRM model in Hunza basin for understanding the hydrologic response to climate change scenarios	Conceptual, degree-day approach; snow cover data are required as model input; flow composition cannot be differentiated.
Schaner et al. [2012]	Estimate contribution of glaciermelt to discharge using energy balance-based single-layer glacier scheme in VIC model. Soil-Vegetation-Atmosphere-Transfer (SVAT)/ Snow-Soil-Vegetation-Atmosphere-Transfer (SSVAT) schemes are included	Two-layer snow scheme, one-layer glacier scheme. Debris-covered glaciers are not accounted. Internal energy of the glacier is not accounted. No glacier dynamics.
Immerzeel et al. [2012b]	Quantify hydrologic response to climate change using TOPKAPI-ETH model. Ice flow mechanism is accounted. Additionally, gravitational snow tranport model to account mass redistribution from avalanching is included explicitly in modeling framework by *Immerzeel et al.* [2013]	Degree-day approach. SVAT/SSVAT schemes are not included.
Zhao et al. [2013]	Couple energly balance-based glacier model to VIC model. SVAT and SSVAT shcemes are included.	Two-layer snow scheme, one-layer glacier scheme. Debris-covered glaciers are not accounted. Internal energy of the glacier is not accounted. No glacier dynamics.
Zhang et al. [2013]	Establish VIC-glacier model by integrating glacier scheme to VIC model. SVAT and SSVAT shcemes are included.	Degree-day scheme for glacier and snow over glacier. Debris-covered glaciers are not accounted. Ice flow dynamics is not considered.
Ragettli et al. [2013]	Quantify the sources of uncertainty from model parameters, climate models, and natural variability of temperature and precipitation on projections of future runoff in Hunza basin using TOPKAPI-ETH model.	Enhanced temperature index approach; SVAT/SSVAT schemes are not included.
Luo et al. [2013]	Inclusion of glacier process in SWAT model	Degree-day model, semidistributed conceptual model; SVAT/SSVAT scheme is not accounted.
Naz et al. [2014]	Integration of ice dynamics to DHSVM model. SVAT and SSVAT shcemes are included. Most advanced hydrologic model with glacier scheme for long-term simulation.	Two-layer snow scheme, one-layer glacier scheme. Debris-covered glaciers are not accounted. Internal energy of the glacier is not accounted (temperature of glacier is constant throughout the year).
This study	Integration of full energy balance-based multilayer snow, multilayer clean glacier and single-layer debris-covered glacier system. Internal energy of the glacier is accounted. SVAT and SSVAT schemes are included.	Dynamics of ice flow is not considered.

[a]Models for individual glaciers are not discussed here.

glacier-fed river basins with different land use characteristics and climates. Comprehensive evaluation of this model at Snow Model Intercomparison Project (SnowMIP) sites [*Shrestha et al.,* 2010, 2012a] revealed that the snow internal processes (e.g., variability of snow density, snow depth and snow water equivalent, liquid water and ice content in each layer, prognostic snow albedo, and snow surface temperature) were accurately simulated. Basin-scale evaluation of the model in the Dudhkoshi region of the Nepal Himalayas demonstrated the model capability for capturing spatiotemporal variations of snow cover across the study area [*Shrestha et al.*, 2012b]. In addition, the model has been used to establish a novel approach to the correction of basin-scale snowfall using remote sensing data [*Shrestha et al.*, 2014]. The modeling framework of this study would be useful for correction of snowfall amount in reanalysis products and atmospheric model outputs, which would contribute to bias correction of precipitation from climate model projections as precipitation bias is the key error in model input for climate change impact assessment studies. Then, the model would be applicable in assessing the impact of climate change in snow- and glacier-dominated river basins for future climate data; however, coupling of dynamics of the ice flow mechanism [e.g., *Naz et al.*, 2014] should be considered for continuous long-term simulations (e.g., 100 or more years). A summary of major contributions and limitations of this study approach in relation to relevant studies is outlined in Table 1.

In the present study, the enhanced integrated modeling system was implemented for the Hunza River basin of the Pakistan Karakoram region at a spatial resolution of 500 m and a temporal resolution of 1 h, at which runoff is mainly contributed from snow and glacier melt water. We illustrate the model capability in simulating discharge and its flow composition (snowmelt runoff, glacier melt runoff, and rainfall runoff contributions to total runoff), seasonal variation of spatial distribution of snow cover, transient snow line,

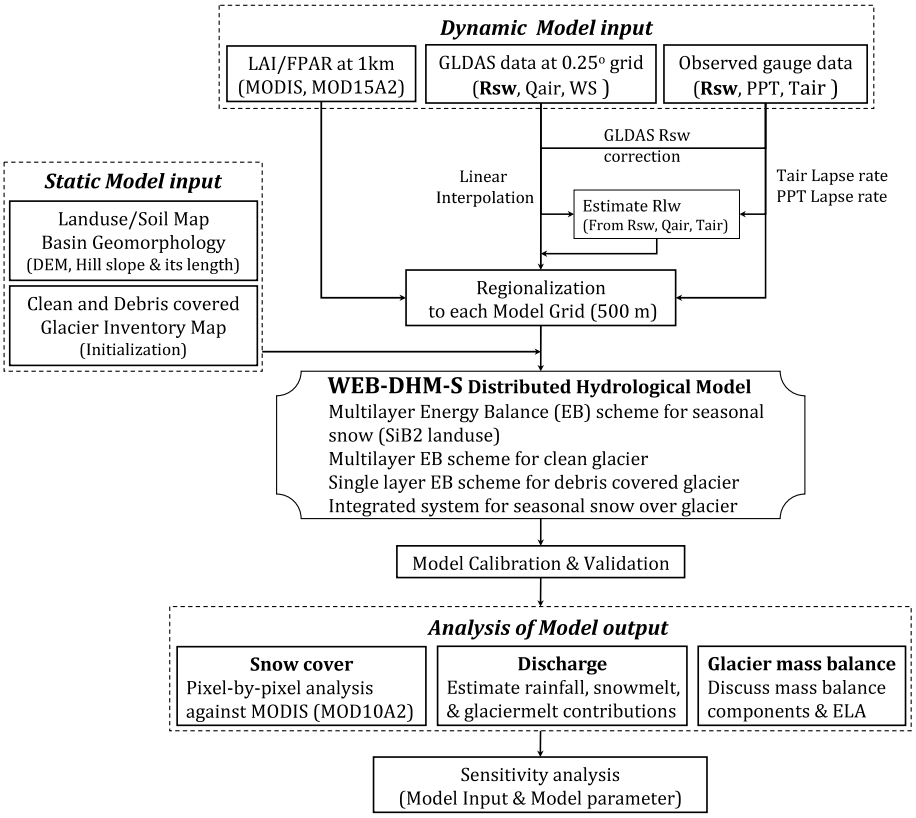

Figure 1. Flow chart of the study approach (R_{sw} and R_{lw} are downward shortwave and longwave radiation; Qair, WS, Tair, PPT, and ELA are specific humidity, wind speed, air temperature, precipitation, and equilibrium line altitude, respectively).

and glacier mass balance (see Figure 1 for flow chart of this study). There were a few studies of this river basin that focused on snow and glacier melt runoff modeling. *Lowe and Collins* [2000] applied a simple conceptual model using a positive degree-day concept, by inputting air temperature and transient snow line data from an AVHRR data set in spring and summer 1989. *Akhtar et al.* [2008] and *Tahir et al.* [2011b] implemented the HBV and SRM hydrologic models, respectively, for addressing the impact of climate change on water resources of the basin. All the aforementioned studies implemented temperature index models, which required snow cover information as input data. These studies were unable to describe physical aspects of the generation of snow and glacier melt runoff and runoff from snow/glacier-free areas. Recent studies [*Ragettli et al.*, 2013; *Pellicciotti et al.*, 2012] used the TOPKAPI-ETH-distributed hydrological model with a degree-day snow/glacier submodule. *Ragettli et al.* [2013] discussed the source of model uncertainty in future runoff projection, concluding that parametric uncertainty exceeds that of other sources of uncertainty, but this effect could be reduced with inclusion of physical descriptions of glaciohydrological processes. The approach developed in this study integrates physical processes which would be able to reduce the source of uncertainty in hydrologic modeling.

The paper is organized as follows. Section 2 describes the study area. Section 3 briefly discusses the structure of the WEB-DHM-S hydrological model, the snowmelt module, and the glacier melt module for debris-covered and debris-free glaciers. Calibration and evaluation methods are presented in section 4. Section 5 presents results of model simulations of discharge and its flow composition, snow cover, snow/glacier states, mass balance, and model sensitivity to uncertainty in input data, model parameters, and change in glacier extent. Concluding remarks are given in section 6.

2. Study Area

The Hunza River Basin (area 13,733 km^2) lies in the high mountainous region of central Karakoram in northern Pakistan, within extent 74°02′–75°48′E and 35°54′–37°05′N. The Hunza is one of the main tributary basins of

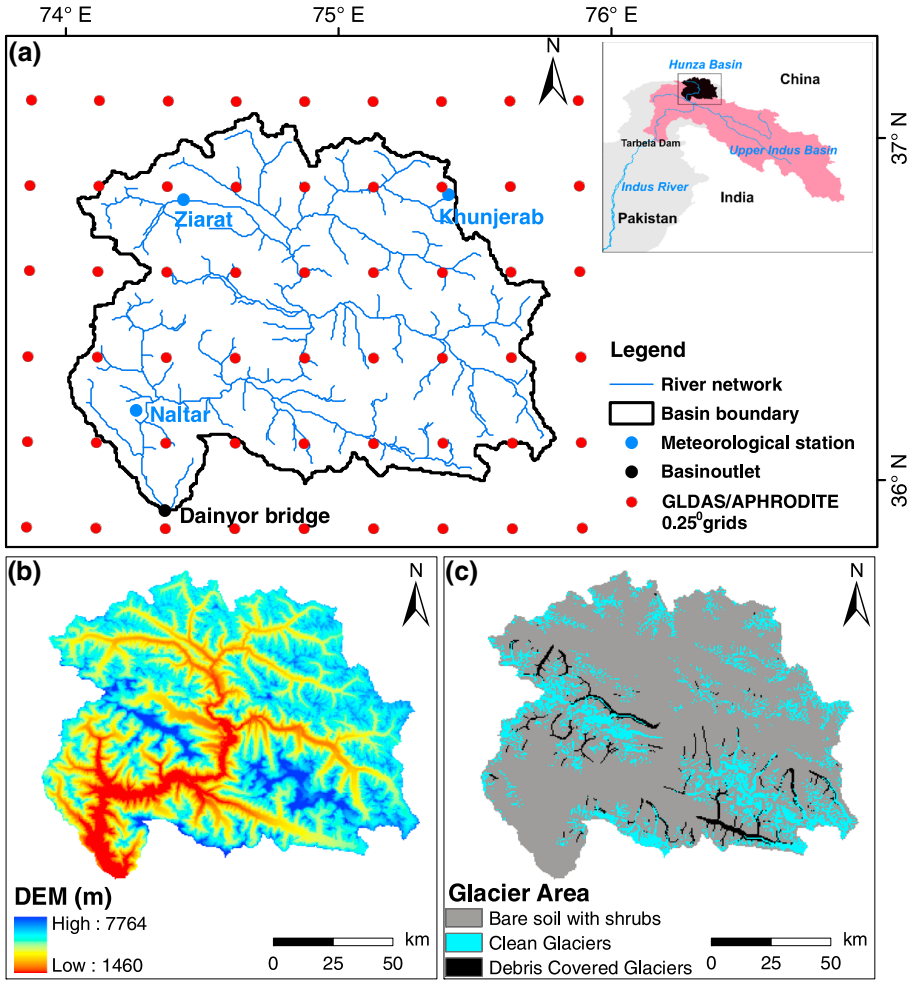

Figure 2. Details of Hunza River Basin. (a) Basin boundary map showing meteorological stations, river network, GLDAS, and APHRODITE (0.25°) grid points, with location map at upper right; (b) digital elevation model (DEM); (c) glacier area (debris covered and clean) in the study area.

the Indus Basin river irrigation system that contributes about 12% of the upper Indus flow, upstream of Tarbela Dam. About 80% of the total inflow into this dam originates from less than 20% of its contributing area, essentially from areas of heavy snowfall and glacierized basins above 3500 m elevation [*Hewitt et al.*, 1989; *Wake*, 1989; *Young and Hewitt*, 1990; *Archer and Fowler*, 2004]. About 50% of the basin area has elevations higher than 4700 m. Figure 2 shows the location and drainage basin of the Hunza River plus hydrological and meteorological stations in the basin, together with digital elevation model (DEM) data and glacier area.

The main physical characteristics of the basin are shown in Table 2. The climate is arid to semiarid and is generally characterized by two seasons, April to September as summer and October to March as winter. The climate is hot in summer at low altitudes, with cold winters and wide variations between temperatures extremes. The basin is dominated by seasonal snow cover in winter, approximately 85%. This figure gradually decreases to about 30% in summer [*Tahir et al.*, 2011a]. The greater part of the basin (90%) is in the rain shadow of the Himalayas, and therefore, summer monsoon precipitation infrequently penetrates the front ranges of the mountains. However, the rain shadow influence weakens northwestward [*Young and Hewitt*, 1990; *Fowler and Archer*, 2006]. The primary source of regional precipitation is of weak intensity during winter and spring, brought by westerly circulations. These westerlies contribute about two thirds of high-altitude snowfall in the Karakoram [*Bookhagen and Burbank*, 2010]. The basin hydrologic regime suggests that river discharge is at a minimum during the snow accumulation period (November through

Table 2. Major Physical Characteristics of the Hunza River Basin

Physical Characteristics	Description
Catchment Area	13,733 km^2
Glacier	2,754 km^2 (20%)
Clean glacier	2,344 km^2 (85% of glacier area)
Debris-covered glacier	410 km^2 (15% of glacier area)
Elevation range	1,460–7,764 m
Catchment area above 4,700 m	50%
Latitude	35°54′ to 37°05′
Longitude	74°02′ to 75°48′
Dominant land use type	Bare soil with shrubs
Catchment outlet gauging station	Dainyor bridge
Mean runoff (1966–2008)	742 mm (eq. 323 $m^3 s^{-1}$)
Mean precipitation (2001–2004)	
Khunjerab (4,730 m)	165 mm
Ziarat (3,669 m)	292 mm
Naltar (2,858 m)	660 mm

early April) and begins to increase during April with a mean temperature increase in the catchment, especially within low-elevation snow-covered areas. Afterward, increment in discharge accelerates as the snow and glaciers begin melting with the rise of air temperature. There is significant correlation (~0.7) between summer (July to September) mean temperature and stream flow [*Archer*, 2003]. The area above 5000 m is considered the most active hydrological part of the basin, where maximum snowfall and accumulation occurs [*Young and Hewitt*, 1990]. All meteorological gauges in this region are below this altitude range, and therefore, the actual amount of precipitation is not known. Details on the spatial variability of precipitation are given in section 3.2.1.

3. Materials and Methods

3.1. WEB-DHM-S Model

The WEB-DHM-S model is a physically based, distributed biosphere hydrological model [*Shrestha et al.,* 2010, 2012a, 2012b] that was developed by coupling the three-layer energy balance snow scheme of SSiB3 and prognostic albedo scheme of BATS with the WEB-DHM [*Wang et al.,* 2009a, 2009b]. The model has the capability to express basin-scale spatiotemporal variabilities of snow density, snow depth, snow water equivalent, liquid water content, ice content, snow albedo, and snow layer temperature in nine biomes with partial to full vegetation coverage, as described in the SiB2 land surface model [*Sellers et al.*, 1996]. The present study is innovative in the development of energy balance-based glacier physics for debris-free clean and debris-covered glaciers to investigate the influence of glaciers on catchment hydrology and the implementation of an integrated system to simulate snow and glacier melt contributions in the Hunza River Basin.

The basin and sub-basins are defined from a DEM using the Pfafstetter system [*Verdin and Verdin*, 1999]. Each sub-basin is divided into a number of flow intervals based on time lags. Each interval contains several model grids. Each model grid is ascribed one land use type and one soil type and is represented as a geometrically symmetric hillslope, a rectangular inclined plane with a defined length and unit width. A land surface submodel is used to compute water and energy fluxes between lower atmosphere and land surface. Then, vertical water distributions (surface storage, subsurface storage, soil moisture, and groundwater profile) and energy distribution (surface and subsurface temperature, sensible and latent heat fluxes) are updated. Surface and subsurface runoffs from model grids in one flow interval are accumulated into a virtual channel leading to the river basin outlet. Flow routing of the basin river network was modeled using the kinematic wave method. Overall model structure is illustrated in Figure 3. Details of the snowmelt and glacier melt module are described in subsequent subsections.

3.1.1. Snowmelt Module for Land

Because water and energy fluxes are computed for nine different biomes (as described in SiB2), snow processes at grids with partial to full coverage of vegetation fraction were considered. Snow intercepted by canopy/vegetation is treated as a single layer, irrespective of its total depth. Subcanopy snowpack is divided into three layers when its depth exceeds 5 cm. For these three layers, the top layer is kept at a fixed depth of 2 cm, the middle layer 20 cm, and the remainder as the bottom layer. Snowpack energy is represented by specific enthalpy, which includes both the internal energy of liquid water or ice and the energy of phase change. The heat budget of the top layer is controlled by surface energy balance and heat conduction from second layer, whereas that of the second and third layers is modulated by heat conduction. The mass budget for each snow layer is calculated accordingly, by consideration of precipitation, direct throughfall, drip fall, evaporation, condensation, compaction,

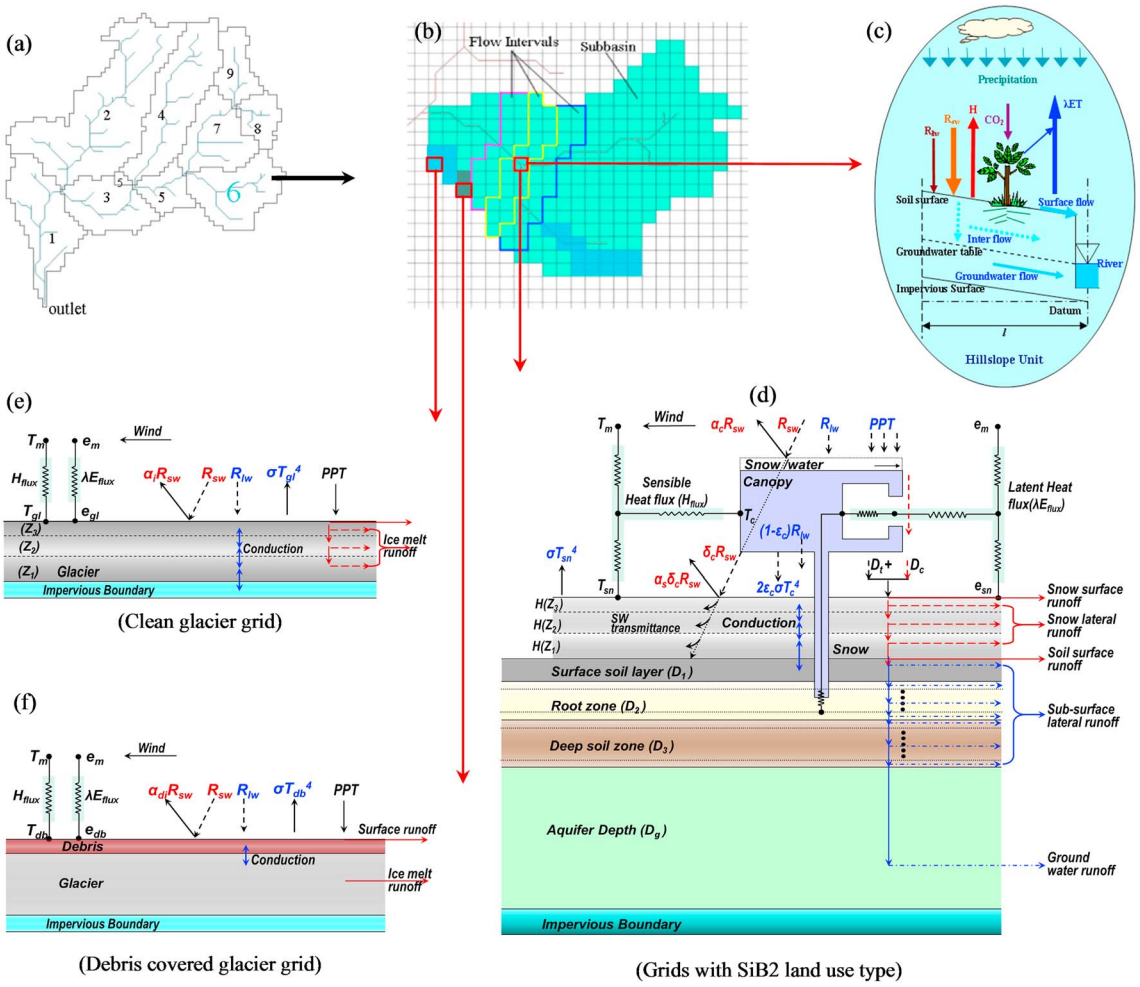

Figure 3. Overall structure of WEB-DHM-S model. (a) Division from basin to sub-basin; (b) subdivision from sub-basin to flow intervals comprising several model grids; (c) description of water transfer from atmosphere to river (a, b, and c; after *Wang et al.* [2009a]); (d) detailed description of vertical three-layer energy balance snow model; (e) detailed description of vertical three-layer energy balance glacier model for debris-free/clean glacier; (f) detailed description of vertical one-layer energy balance glacier model for debris-covered glacier, in which T is temperature, $e(T)$ is vapor pressure at T, R_{sw} and R_{lw} are downward shortwave and longwave radiation, H and λE are sensible and latent heats, and ε, δ, and α are emissivity, transmittance, and reflectance, respectively. Subscript c refers to canopy, g to soil surface, sn to snow surface, gl to clean glacier surface, db to debris-covered glacier surface, and m to the reference height (after *Shrestha et al.* [2014]).

liquid water retention, snowmelt runoff, and infiltration into underlying layers. A schematic of model processes in the WEB-DHM-S is presented in Figure 3d.

The energy budget equation for the canopy is

$$C_c \frac{\partial T_c}{\partial t} = R_{nc} - H_c - \lambda E_c, \tag{1}$$

where C_c ($\mathrm{Jm^{-2}\,K^{-1}}$) is the effective heat capacity, T_c is canopy temperature, and R_{nc}, H_c, and λE_c ($\mathrm{Wm^{-2}}$) are net radiation, sensible heat, and latent heat flux for the canopy, respectively. WEB-DHM-S uses a two-stream approximation scheme for radiation transfer in the canopy. The equation for enthalpy is

$$\begin{aligned} \frac{\partial H(Z_j)}{\partial t} &= -\frac{\partial G_{sn}(Z_j)}{\partial z} \\ H(Z_j) &= C_v(Z_j) \times \{T_{sn}(Z_j) - 273.16\} - f_{\mathrm{ice}}(Z_j) \times h_v \times \rho_s(Z_j) \\ G_{sn}(Z_j) &= \begin{cases} R_{nsn} - H_{sn} - \lambda E_{sn} + G_{pr} & \text{at snow surface } (j=3) \\ K(Z_j)\dfrac{\partial T_{sn}(Z_j)}{\partial Z} + SW_{sn}(Z_j) & \text{within snow layers } (j=2,1) \end{cases} \end{aligned} \tag{2}$$

Here, H (Jm^{-3}) is the volumetric enthalpy of water, Z_j is snow depth of layer j, G_{sn} (Wm^{-2}) is heat flux through the snow layer, C_v ($Jm^{-3}\,K^{-1}$) is the mean snow volumetric heat capacity, T_{sn} (K) is snow temperature, f_{ice} is the mass fraction of ice in the j^{th} snow layer, h_v (Jkg^{-1}) is the latent heat of fusion for ice, and ρ_s ($kg\,m^{-3}$) is the bulk density of snow. R_{nsn} (Wm^{-2}), H_{sn} (Wm^{-2}), λE_{sn} (Wm^{-2}), G_{pr} (Wm^{-2}), K ($Wm^{-1}\,K^{-1}$), and SW_{sn} (Wm^{-2}) are net radiation, sensible heat, latent heat flux, thermal energy from rain at the snow surface, and thermal conductivity of snow and shortwave radiation flux absorbed by the snow layer, respectively. Snow albedo for the canopy is computed using a two-stream approximation model [*Sellers et al.*, 1996]. Snow albedo of the land surface is computed for visible and near-infrared spectral bands, with adjustments for illumination angle and snow age [*Dickinson et al.*, 1993]. Temporal variations of ground temperature (T_g) and deep soil temperature (T_d) are predicted using a force-restore method. An implicit backward numerical scheme is used to solve rapidly varying variables (i.e., T_c and $T_{sn}(Z_3)$) simultaneously by computing temperature increments for the physics time step. An explicit forward numerical scheme is used to solve slowly varying variables (i.e., $T_{sn}(Z_2)$, $T_{sn}(Z_1)$, T_g, and T_d). Details of the snow energy balance equations were given by *Shrestha et al.* [2010, 2012b].

The mass balance for snow is represented by the relative change of snow mass (liquid water and ice content), which is governed by precipitation (snow/rain), compaction, melting, infiltration into the underlying snow layer/soil, evaporation/sublimation, and runoff. The mass balance equation for the canopy is

$$\frac{\partial M_{csn}}{\partial t} = P - D_t - D_c - \frac{E_{ci}}{\rho_w}, \tag{3}$$

where M_{csn} is snow water equivalent stored on the canopy surface (m), P is precipitation rate ($m\,s^{-1}$), D_t is canopy throughfall rate ($m\,s^{-1}$), D_c is canopy drainage rate ($m\,s^{-1}$), E_{ci} is evaporation rate from canopy interception stores ($kg\,m^{-2}\,s^{-1}$), and ρ_w is density of liquid water ($kg\,m^{-3}$). The mass balance equation for subcanopy snow is

$$\frac{\partial M_{sn,j}}{\partial t} = \begin{cases} D_t + D_c - IF_{j,sn} - R_{j,sn} - \dfrac{E_{sn}}{\rho_w}, & \text{at snow surface } (j=3) \text{ over land} \\ P - IF_{j,sn} - R_{j,sn} - \dfrac{E_{sn}}{\rho_w}, & \text{at snow surface } (j=3) \text{ over glacier} \\ IF_{j+1,sn} - IF_{j,sn} - R_{j,sn}, & \text{within snow layers } (j=2,1) \end{cases}, \tag{4}$$

where $M_{sn,j}$ (m) corresponds to SWE at snow layer j, $IF_{j,sn}$ (ms^{-1}) is actual liquid water infiltration flux at the interfaces, $R_{j,sn}$ (ms^{-1}) is runoff from the lower interface, and E_{sn} (ms^{-1}) is the combined evaporation and sublimation rate. Three snow compaction processes, namely, destructive metamorphism, densification because of snow overburden, and compaction by snowmelt, are parameterized following *Jordan* [1991].

3.1.2. Snowmelt Module for Glacier

The glacier in the model is generally treated as clean ice/debris-covered ice without snow. When the glacier surface is covered with new snow, an interface is created between that snow and ice. The three-layer snow algorithm discussed in section 3.1.1 was adopted for new snow with altered lower interface. That interface would be snow-glacier and snow-debris for clean and debris-covered glaciers, respectively. The interface alters available energy in the third layer from/to the glacier underneath, which changes the enthalpy of all three snow layers. Total outflow from the snow layers is the water equivalent input to the glacier surfaces in the glacier melt module (equation (4)).

3.1.3. Glacier Melt Module

The glacier melt module includes two different approaches to deal with clean and debris-covered glaciers. The three-layer energy balance model is used for clean ice, whereas a single-layer surface energy balance based on thermal resistance is used for simulation of ice melt from glaciers underneath the debris. The entire model grid is assumed to be covered by debris-free or debris-covered ice. If snow accumulation/ablation occurs on these glaciers, it is assumed that the glacier is either completely snow-covered or completely snow free.

3.1.3.1. Clean Glacier

The model structure of the three-layer snowpack module was implemented for the computation of water and energy fluxes over glaciers using the ice thermal conductivity, ice volumetric heat capacity, ice density, and ice albedo in equation (2). Heat exchange for the lower layer interface is the heat between the glacier and bedrock. Ice albedo was set to 0.4 [*Paterson*, 1994] for the computation of upward shortwave radiation and was assumed

constant [*Hock and Holmgren*, 2005; *Klok and Oerlemans*, 2002]. Major model processes are schematized in Figure 3e. Mass balance for a clean glacier is controlled by snowfall/rainfall, melt outflow from snow above the glacier, transformation of snow into ice, glacier melt and its internal refreezing, and runoff that exits glacier storage. The mass balance equations are defined as

$$\frac{\partial M_{\text{cleang}l,j}}{\partial t} = \begin{cases} IF_{1,sn} - IF_{j,gl} - R_{j,gl} & \text{top layer } (j=3), \text{ if snow exists} \\ P - IF_{j,gl} - R_{j,gl} - \dfrac{E_{gl}}{\rho_w} & \text{top layer } (j=3) \\ IF_{j+1,gl} - IF_{j,gl} - R_{j,gl} & \text{intermediate layer } (j=2) \\ IF_{j+1,gl} - R_{j,gl} & \text{bottom layer } (j=1) \end{cases} \tag{5}$$

Here, $M_{\text{cleang}l,j}$ (m) corresponds to the water equivalent at clean glacier layer j. During mass balance, calving processes and avalanches caused by glacier surges are not considered. Snow atop glaciers is converted to permanent ice once its density exceeds 800 kg m^{-3}.

3.1.3.2. Debris-Covered Glacier

The surface energy balance over a debris surface is completely different than that over clean ice, because debris surface temperature can be several degrees higher than the freezing temperature of clean ice. The single-layer surface energy balance scheme was developed to simulate melt of debris-covered glaciers (Figure 3f). Energy balance closure at the debris surface is expressed by

$$\begin{aligned} G_{\text{debris}} &= R_{n(d)} - H_{(d)} - \lambda E_{(d)} + G_{pr(d)} \\ G_{\text{debris}} &= K_d \left(\frac{T_{db} - T_{gl}}{h_{\text{debris}}} \right) = \frac{T_{db} - T_{gl}}{R_{th}} \end{aligned} \tag{6}$$

Here, $R_{n(d)}$, $H_{(d)}$, $\lambda E_{(d)}$, and $G_{pr(d)}$ (all in Wm^{-2}) are net radiation, sensible heat, latent heat flux, and thermal energy from rain at the debris surface, respectively. G_{debris} is the conductive heat flux into the debris layer. The debris albedo was set to 0.15 [*Paterson*, 1994] and assumed spatiotemporally constant; in fact, it may vary from 0.1 to 0.2. G_{debris} is a function of the temperature gradient between upper and lower surfaces of the debris layer and its thermal resistance. As defined in equation (6), this gradient is assumed to be linear, following previous works [*Nakawo and Young*, 1981; *Nicholson and Benn*, 2006]. R_{th} (m^2 KW^{-1}) is thermal resistance of the debris layer, which is the ratio of debris thickness (h_d) to thermal conductivity (K_d) of the layer [*Nakawo and Young,* 1981, 1982]. T_{gl} is temperature at the ice-debris interface, which is assumed constant at 0 °C [*Nakawo and Young*, 1981; *Nicholson and Benn*, 2006]. The debris surface temperature (T_{db}) is calculated by numerical iteration of the above surface energy balance equation. From the iterated value of T_{db}, G_{debris} is computed for the prescribed thermal resistance of a debris layer in equation (6). The glacier melt rate $M_{\text{debris}gl}$ (ms^{-1}) under the debris is then calculated from available conductive energy, ice density (ρ_i), and latent heat of fusion (h_v):

$$M_{\text{debris}gl} = \frac{G_{\text{debris}}}{\rho_i h_v} \tag{7}$$

3.1.4. Runoff Generation

Once the energy and water balance calculations are made for each model grid (snow-covered and snow-free land as well as glaciers), water from surface and subsurface runoff is redistributed laterally considering topographic effects using grid-hillslope discretization. Then, this water is routed through the river network using kinematic wave flow routing following methods used in WEB-DHM [*Wang et al.*, 2009a].

For snow-covered and snow-free land grids, the surface and subsurface water flux movements are linked through infiltration, evapotranspiration, and saturation capacity of the unsaturated zone, which follows the solution for vertical one-dimensional soil water movement using the Richards equation. This vertical flow in the unsaturated zone contributes to saturated excess and recharge of groundwater. Lateral flows in the unsaturated zone directly enter streams along hill slopes and contribute to runoff. Therefore, subsurface runoff from a hill slope unit includes not only exchanges between groundwater and river (computed through Darcy's law) but also interflows from the unsaturated zone. Available surface water is directed toward surface runoff after it meets the maximum surface water detention. The surface runoff is then described by steady constant sheet flow using Manning's equation.

Table 3. Summary of Data Set

Data	Spatial Resolution	Temporal Resolution	Source
DEM	Grid (90 m)	Fixed	SRTM
Meteorological data (wind speed, specific humidity, downward shortwave radiation)	Grid (0.25°)	3-hourly	Global Land Data Assimilation System (GLDAS)
Precipitation	Grid (0.25°)	Daily	Asian Precipitation–Highly Resolved Observational Data Integration Towards Evaluation of Water Resources (APHRODITE)
Air temperature, shortwave radiation, and precipitation at Natar, Ziarat and Khunjerab stations	Point	Daily	Water and Power Development Authority (WAPDA)
Soil type	Grid (9 km)	Fixed	FAO
Land use	Grid (1 km)	Fixed	USGS
Glacier cover	Coverage	Fixed	International Center for Integrated Mountain Development (ICIMOD)
LAI	Grid (1 km)	8 day average	MODIS Terra (MOD15A2)
FPAR	Grid (1 km)	8 day average	MODIS Terra (MOD15A2)
Snow cover	Grid (500 m)	8 day maximum snow extent	MODIS Terra (MOD10A2)
Discharge at Dainyor bridge	Point	Daily	Surface Water Hydrology Project—WAPDA

For glacier grids, it is assumed that no soil columns exist below the glacier mass, and thus, the glacier melt and rainwater do not pass through the infiltration and vertical water redistribution as they do for other land use type grids. Thus, the subglacial drainage system is replicated by introducing the concept of a storage constant for outflow from the glacier grid. The discharge per unit width (q) at hourly time interval is given by

$$q(t_1) = q(t_0)e^{-1/k} + M_{\text{clean(debris)}gl}(t_1)\left\{1 - e^{-1/k}\right\}, \tag{8}$$

where t_1 is the current time step and t_0 the previous time step, $M_{\text{clean(debris)}}$ is water available from the clean/debris glacier grid at the current time, and k is the storage constant. The value of k varies from 4 to 40 for ice [*Hock and Holmgren*, 2005; *Sicart et al.*, 2011; *Ragettli et al.*, 2013]. The lateral flow from each model grid is then routed via the kinematic wave method.

3.2. Input Data Set

Geomorphological characteristics (hill slope and hill slope length) of the basin are obtained by processing a 90 m resolution DEM. Subgrid parameterizations are aggregated into a 500 m resolution model grid. The DEM is from the Shuttle Radar Topography Mission (SRTM) of NASA (http://srtm.csi.cgiar.org/). Land use static data at 1 km from the U.S. Geological Survey were modified based on glacier coverage data from the International Center for Integrated Mountain Development (ICIMOD). The glacier inventory coverage was produced by a semiautomated object-based classification method based on Landsat 5-MSS and Landsat 7-ETM+ images from 2005 ± 3 years and high-resolution images of Google Earth, in combination with SRTM DEMs [*Bajracharya and Shrestha*, 2011]. Glacier thickness values were generated by using a scaling formula based on the area of glacier; however, the value is highly uncertain [*Bajracharya and Shrestha*, 2011]. Static vegetation parameters included morphological, optical, and physiological properties of various vegetation types as defined in the SiB2 model [*Sellers et al.*, 1996]. Soil parameters were sourced from the globally consistent digital soil data of the Food and Agriculture Organization [*FAO*, 2003], including saturated soil moisture content, residual soil moisture content, saturated hydrologic conductivity for the soil surface, and van Genuchten parameters [*van Genuchten*, 1980]. Dynamic vegetation forcing included Leaf Area Index (LAI) and Fraction of Photosynthetic Active Radiation (FPAR). LAI and FPAR were obtained from the Moderate Resolution Imaging Spectroradiometer (MODIS), aboard Terra satellite. These data are 8 day composites of MOD15A2 version 5.0 products at 1 km spatial resolution.

The three meteorological stations were widely dispersed across the basin and are high-altitude sites of the Water and Power Development Authority (WAPDA) of Pakistan (Figure 2a and Table 2). Elevations of

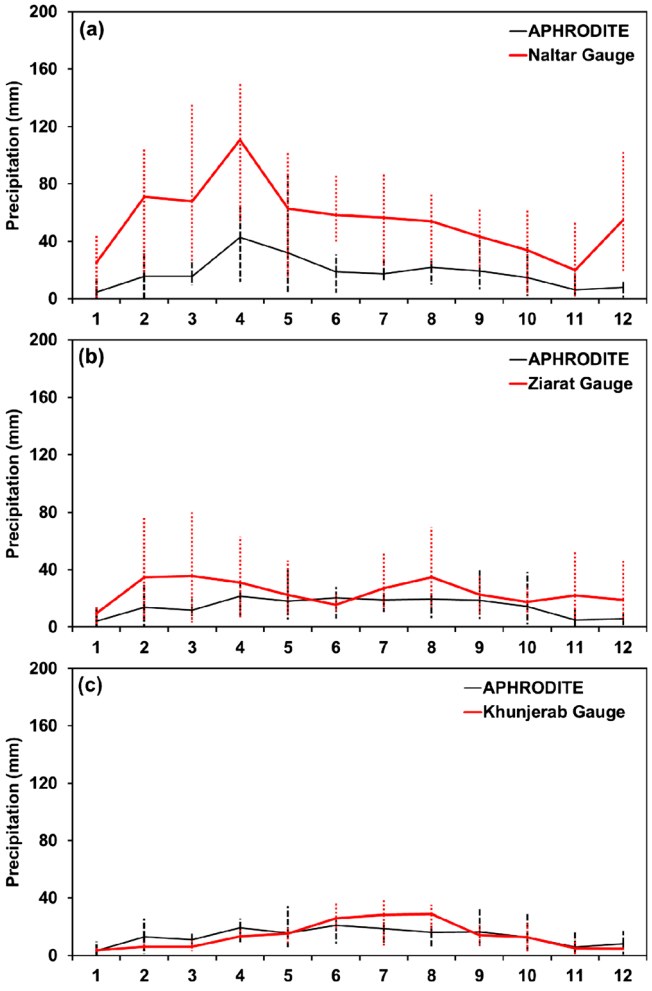

Figure 4. Comparison of monthly total values of observed and APHRODITE precipitation data averaged over 2001–2004 at (a) Naltar, (b) Ziarat, and (c) Khunjerab stations. Upper and lower boundaries represent maximum and minimum values of precipitation during 2001–2004.

WAPDA stations in the basin were from 2858 m to 4730 m. Maximum and minimum air temperature, total solar radiation, and total precipitation were available daily at these three stations. Meteorological variables from the Global Land Data Assimilation System (GLDAS) were also used. The GLDAS data sets have 3 h temporal resolution and 0.25° spatial resolution and are model outputs from the Noah land surface model in the GLDAS framework. Moreover, applicability of the APHRODITE (Asian Precipitation–Highly Resolved Observational Data Integration Towards Evaluation of Water Resources) precipitation data set was tested. APHRODITE is a long-term gridded (0.25°) daily precipitation data set (1961–2007) for Asia that combines gauge and satellite data [*Yatagai et al.*, 2012]. A summary of the data set is provided in Table 3.

Given the harsh and rugged terrain of the study area, field observations of debris thickness are difficult. Thermal resistance for glaciers there has not been assessed. Previous studies near the Hunza River Basin show that this resistance varies substantially with debris depth, e.g., from 0.02 to 0.08 m^2KW^{-1} for debris thickness of 1–5 cm at Bagrot Valley in the Karakoram [*Mayer et al.*, 2010]. Through the use of satellite remote sensing and observed meteorological data at Baltoro Glacier, *Mihalcea et al.* [2008] estimated that the majority of debris-covered glaciers have thermal resistance from 0 to 0.1 $m^2\,KW^{-1}$, but maximum values of 0.6 $m^2\,KW^{-1}$ were calculated at the terminus, where the debris was 1–3 m thick. The present study used a spatiotemporally constant value of thermal resistance, which was the average from *Mayer et al.* [2010].

3.2.1. Spatial Variability of Precipitation

Precipitation is the most important forcing data in distributed hydrologic modeling of a mountainous river basin [*Garen and Marks*, 2005; *Shrestha et al.*, 2014], and thus, uncertainty in its spatial distribution would strongly affect the results of hydrologic simulation. Given the availability of only three stations in the study area, it is challenging to determine the spatial variability of precipitation; however, the gridded APHRODITE data set is a possibility [*Tahir et al.*, 2011b]. Seasonal variation of monthly total precipitation averaged over 2000–2004 at Naltar, Ziarat, and Khunjerab stations and their comparison to corresponding APHRODITE grid data are presented in Figures 4a–4c. Total annual precipitation at Naltar (2858 m) was 660 mm, about four times that (165 mm) at Khunjerab (4730 m). The gauge at Ziarat (3669 m) received about 292 mm annually. Precipitation in February, March, and April was greater than in other months at Naltar, with more variability. Ziarat has the most precipitation in February, March, and August. Khunjerab records greater precipitation in summer. These results indicate that the APHRODITE data set has substantial underestimation at Naltar, although the seasonality is well represented. At Ziarat, the underestimation was less than at Naltar, but the performance of APHRODITE in representing seasonality was poor.

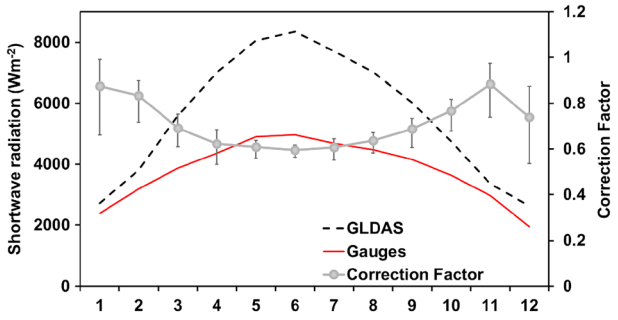

Figure 5. Comparison of monthly average daily total downward shortwave radiation (Wm^{-2}) at gauges and GLDAS grids during 2001–2004. Upper and lower boundaries represent maximum and minimum values of correction factor for shortwave radiation among the gauges.

There was strong correlation in terms of seasonality and total amount at Khunjerab. The reliability of APHRODITE data in Hunza River Basin was very poor. An indicator was introduced additionally to represent the reliability of interpolated daily precipitation fields by the data provider. This indicator was calculated for each 0.25° cell via the proportion of 0.05° cell(s) containing station(s). Analysis of this indicator indicates that this ratio was zero throughout the basin, implying that the observed station values have not been used in the study area. The precipitations obtained were only interpolated values from stations outside the basin, supplemented by satellite precipitation data. Moreover, these data do not consider the spatial heterogeneity and elevation effect in the considered grid. The APHRODITE data set should therefore be corrected in the study area for hydrologic simulation, but this is beyond the scope of this paper.

Because the meteorological gauges were located below the most active hydrologic region, the actual amount of precipitation in the study area is unknown. Previous studies suggest that annual precipitation above 5000-m elevation is in the order of 1800–2000 mm [*Hewitt et al.*, 1989; *Wake*, 1989; *Winiger et al.*, 2005]. *Hewitt* [2005, 2014] indicated a 5–10-fold increase in precipitation between glacier termini around 2500 m and accumulation zones above 4800 m in the Karakoram region, with maximum precipitation between 5000 and 6000 m. Thus, inclusion of a vertical precipitation lapse rate according to the altitudinal gradient is critical to glaciohydrological modeling in the region. This lapse rate would vary by model, based on its structure, parameter settings, and study area. For instance, it was shown to be 0.04% m^{-1} (factor of 1.4 increase per kilometer elevation difference) in the Langtang Basin of the Nepalese Himalaya [*Immerzeel et al.*, 2012a] and 0.21% m^{-1} [*Immerzeel et al.*, 2012b] and 0.4% m^{-1} [*Ragettli et al.*, 2013] in the Hunza River Basin. In the present study, the altitudinal gradient of precipitation was employed in angular distance weight (ADW) interpolation method [*New et al.*, 2000] following *Shrestha et al.* [2014].

$$P_{\text{grid}}(z) = \frac{1}{\sum_{i=1}^{ng} W_i}\left[\sum_{i=1}^{ng} P_{\text{gauge}}(z_i) * W_i * [1 + (z - z_i) * C_f]\right] \quad \text{for} \quad C_f = \begin{cases} C_{f\text{rain}} & (T_{\text{grid}} > T_{th}) \\ C_{f\text{snow}} & (T_{\text{grid}} \le T_{th}) \end{cases} \tag{9}$$

Here, P_{grid} (z) is precipitation (m) at elevation z (m), P_{gauge} (z_i) is observed precipitation at gauge i at elevation z_i (m), W_i is the angular distance weight factor for gauge i, ng is the total number of nearest-neighbor gauges contributing to the grid point during interpolation, $C_{f\text{snow}}/C_{f\text{rain}}$ is a calibration parameter (m^{-1}) for the orographic correction factor of snowfall/rainfall, and T_{grid} and T_{th} are air temperature at model grid and threshold temperature for separation of snowfall/rainfall. The $C_{f\text{snow}}/C_{f\text{rain}}$ is assigned to four elevation bands: (a) less than 4500 m, (b) 4500–5000 m, (c) 5000–6000 m, and (d) greater than 6000 m. $C_{f\text{snow}}/C_{f\text{rain}}$ values are 0.00075, 0.0015, 0.003, and 0.0025 m^{-1}, respectively, for these bands.

3.2.2. Spatial Variability of Meteorological Variables

Downward shortwave radiation and air temperature data sets are key forcing data for the computation of energy balance fluxes. Shortwave radiation data from GLDAS has biases, and thus, great care should be taken before implementation using these data [*Wang et al.*, 2011; *Decker et al.*, 2012]. Gridded values of GLDAS downward shortwave radiation were corrected based on observed values at the three WAPDA stations in the basin (see Figure 2 for GLDAS grids). Daily total values of shortwave radiation were obtained from aggregation of the 3-hourly GLDAS data set. Data from a 4 year (2001–2004) period were analyzed. Monthly variations of observed and GLDAS shortwave data are presented in Figure 5. This shows that GLDAS strongly overestimated solar radiation in summer (May through September). A correction factor for the three stations was determined and distributed on each grid using ADW interpolation.

Air temperature at each grid was estimated using the observed lapse rate from temperature measurements at Naltar and Khunjerab stations. The daily lapse rate varied from 0.23 to 0.92 °C km^{-1} (2001–2004 average was 0.61 °C km^{-1}). Specific humidity, wind speed, and air pressure were directly used from GLDAS. Linear interpolation was used to downscale the 0.25° gridded GLDAS data to 500 m × 500 m grids. Downward longwave radiation was then estimated from air temperature, specific humidity, pressure, and shortwave radiation, using a relationship between the latter and longwave radiation [*Crawford and Duchon*, 1999].

3.3. Evaluation Data Set

Observed daily discharge at Dainyor Bridge and MODIS-derived snow cover extent were used to evaluate model performance. Although discharge data were available from 1966 to 2008, the model was evaluated for the period 2002–2004 due to the constraints of data availability. Meteorological data (precipitation, air temperature, and solar radiation) were available from 1995. MODIS snow data were available from the summer of 2000, and GLDAS forcing data were available from 2000. Sensor for precipitation failed in November to December of 2005 and in September to December of 2006, and discharge was missing in 2007. Thus, 3 years of hydrological simulation (2002–2004) was selected in this study for the evaluation of the model. The discharge data were obtained from the surface water hydrology project of WAPDA. The snow cover extent data were from the 8 day maximum snow extent data set of MODIS, aboard the Terra satellite (MOD10A2). This is an 8 day composite snow cover product with 500 m spatial resolution, derived from 8 day periods of the MOD10A1 daily product. MOD10A2 represents the maximum extent of snow cover over 8 days. In this data set, a pixel is classified as cloud only when it is continuously cloud covered during all 8 days. The pixel is classified as snow covered if snow cover is observed on any of the 8 days. The 8 day product acts as a temporal filter of MOD10A1 data, minimizing the effect of cloud. The study area comprises two tiles (h23V05 and h24V05), which were obtained from the NASA Earth Observing System Data and Information System (http://reverb.echo.nasa.gov). These MODIS tiles were first mosaicked and projected into the WGS 1984 UTM ZONE 43 N system and then resampled to a model grid resolution via the MODIS Reprojection Tool [*MRT*, 2011].

4. Model Calibration and Evaluation

Although the WEB-DHM-S model is physics based, it contains a few parameters that can be optimized to achieve better simulation results with respect to observations. The most important parameters include visible albedo of fresh snow, albedo of clean ice, saturated hydraulic conductivity of soil, hydraulic conductivity anisotropic ratio, and precipitation correction factor. These parameters are optimized through an automatic search algorithm called Shuffled Complex Evolution–University of Arizona (SCE-UA) [*Duan et al.*, 1992]. Initial conditions of soil moisture and groundwater storage are obtained by running the model several times until hydrologic equilibrium is reached. The objective function for optimization is for achieving minimum error in discharge simulation through the use of Nash-Sutcliffe efficiency (NSE) [*Nash and Sutcliffe*, 1970] and relative volume error (RVE). These are defined as

$$NSE = 1 - \frac{\sum_{i=1}^{N} (Q_{oi} - Q_{si})^2}{\sum_{i=1}^{N} (Q_{oi} - \overline{Q}_o)^2} \tag{10}$$

$$RVE = \frac{\sum_{i=1}^{N} (Q_{si} - Q_{oi})}{\sum_{i=1}^{N} Q_{oi}}, \tag{11}$$

where Q_{oi} is observed discharge, Q_{si} is simulated discharge, and $\overline{Q}_o$ is the mean discharge observed over the simulation period with N number of days. The most important model parameters are given in Table 4.

Model-simulated snow-covered area (SCA) was evaluated by pixel-to-pixel analysis of its comparison with MODIS-derived SCA. The MODIS data provide information on absence or presence of snow, whereas the model provides the amount of snow or ice (in water equivalent) at each grid. Since the MODIS product

Table 4. Model Parameters

Symbol	Parameters	Value	Source
α_{vis0}	albedo of fresh snow in visible band	0.85	Optimization
α_{nir0}	albedo of fresh snow in near-infrared band	0.65	*Yang et al.* [1997]
α_{ice}	Albedo of clean glacier	0.40	Optimization
α_{debris}	Albedo of debris over glacier	0.15	Optimization
k_{ice}	Storage constant for glacier grid	40	Optimization
$K_{satsoil}$	Saturated hydraulic conductivity for soil surface	0.048 mh^{-1}	*FAO* [2003]
K_g	Groundwater hydraulic conductivity	0.001 mh^{-1}	*Yang et al.* [2004]
$K_{satsnow}$	Saturated hydraulic conductivity for snow	36.0 mh^{-1}	*Shrestha et al.* [2012a]
T_{th}	Rain/snow threshold temperature	1.0 °C	This study
R_{th}	Thermal resistance of debris cover	0.042 $m^2 KW^{-1}$	*Mayer et al.* [2010]
anik	Hydraulic conductivity anisotropic ratio	3.0	Optimization
C_f	Calibration parameter for precipitation correction factor	0.00075–0.0025 m^{-1}	Optimization

differentiate snow and ice together from other land use, bare ice and ice underneath debris are treated as SCA in the model. Absence/presence of snow in the model simulation is determined by setting model grids with snow depth greater than 4 cm to be "snow covered" [*Shrestha et al.*, 2014; *Wang et al.*, 2008; *Klein and Barnett*, 2003]. Based on 2×2 contingency table analysis of snow pixels between MODIS and the model, three indices were used to quantify bias and accuracy of the model (Table 5). These are model overestimation error (M_{OE}), model underestimation error (M_{UE}), and model accuracy (M_{AC}).

5. Results and Discussion

A series of simulations were designed to evaluate the necessity of integration of the glacier model into the current WEB-DHM-S and uncertainty of model input data and parameters. Considering the availability of the observed hydrometeorological and MODIS satellite data, 3 years of hydrological simulation (2002–2004) was carried out. Model performance was first investigated with respect to the calibration period, the hydrologic year 2001–2002. The model was then validated in 2003 and 2004. First, spatial distribution of precipitation is discussed. Second, the evaluation of the model results against observed discharge and MODIS snow cover is discussed. Third, results of snow/glacier states and net mass balance are discoursed. Finally, the sensitivity of model results versus its input and parameters are quantitatively presented, along with seasonal sensitivity of NMB and runoff against monthly perturbations of air temperature and precipitation.

5.1. Spatial Distribution of Precipitation

The spatial distribution of total precipitation (October through September) and ratio of snowfall to total precipitation are portrayed in Figures 6a and 6b for 3 consecutive years. One sees that the northern side of Batura Glacier receives much less precipitation than its southern side. Such a distribution was speculated by previous studies [*Winiger et al.*, 2005; *Immerzeel et al.*, 2012b]. This glacier acts as a precipitation-dividing "wall" between the southern and northern Hunza River Basin. Total precipitation is less than 100 mm at low elevation but exceeds 3000 mm at high elevation, resulting in a very nonuniform spatial pattern. Interannual variability of this spatial distribution was not apparent. Basin average precipitation is 1238 mm yr^{-1}, of which snowfall accounts for 1085 mm and rainfall 152 mm. This average is higher than the ~836 mm estimated by *Immerzeel et al.* [2012b]. The spatial distribution of the ratio of snowfall to total precipitation was about 0.3–0.5 on the valley side and 0.8–1.0 on the ridge side. Hypsometric analysis gives ratios of 0.50, 0.65, 0.73, 0.87, 0.96, and 1.0 for elevations <3500, 3500–4000, 4000–4500, 4500–5000, 5000–5500, and >5500 m in the year 2002. The ratio decreased to 0.44 and 0.38 at grids with elevation <3500 m in the years 2003 and 2004,

Table 5. Contingency Table Used to Compute Evaluation Indices

	MODIS : Snow	MODIS : No Snow
MODEL : Snow	a	b
MODEL : No Snow	c	d

Model Overestimation Error (M_{OE}) = b/(a + b + c + d)
Model Underestimation Error (M_{UE}) = c/(a + b + c + d)
Model Accuracy (M_{AC}) = a + d/(a + b + c + d)

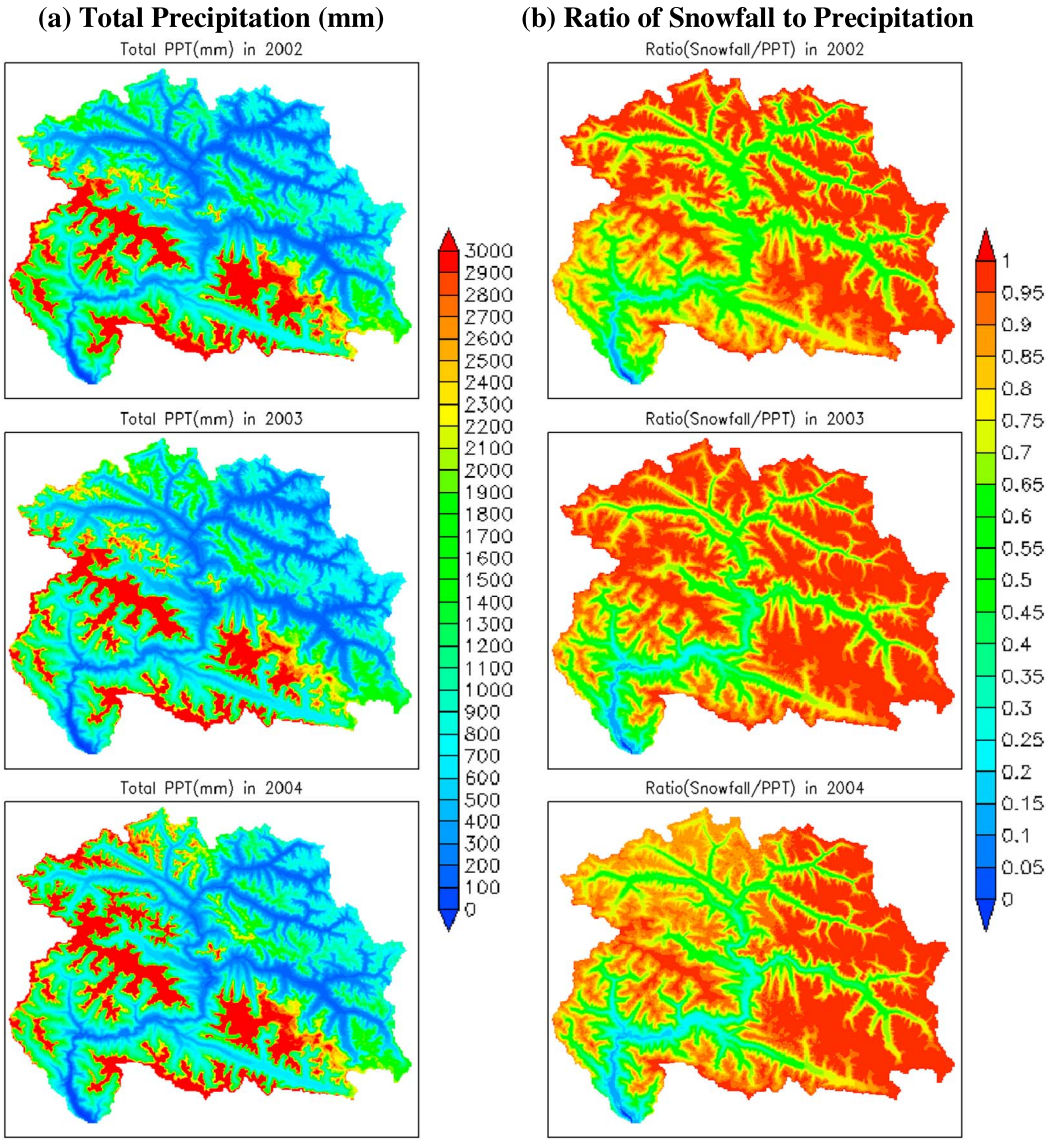

Figure 6. Spatial distribution of (a) total accumulated precipitation (October through September) in years 2002, 2003, and 2004; and (b) ratio of snowfall to precipitation in those years.

respectively. In the elevation bands 3500–4000 m and 4000–4500 m, the ratios increased to 0.66 and 0.79 in 2003, respectively, and were 0.64 and 0.76 in 2004. The ratio of snowfall to total precipitation did not vary significantly above 5000 m.

5.2. Discharge Simulation and Flow Composition

A comparison of observed daily discharge with simulated discharge at Dainyor Bridge (basin outlet) over 3 hydrologic years (2002–2004) is shown in Figures 7a–7c. In the calibration year (2002), the discharge simulation is in good agreement with observations, with NSE of 0.96, RVE of +0.03, and coefficient of determination of 0.98 (Table 6). Discharge in winter was low and nearly constant at ~45 cumecs and slowly increased from mid-April because of the onset of seasonal snowmelt from low-elevation areas. Once the temperature warms, snow atop the glaciers begins to melt. After this snow completely melts, glacier melt begins. The discharge maximizes around August. This mostly comes from the melt of snow and glaciers, because precipitation in the summer monsoon is very slight in the region. There were many large fluctuations of discharge in June and July, in response to daily variations of air temperature. In 2002,

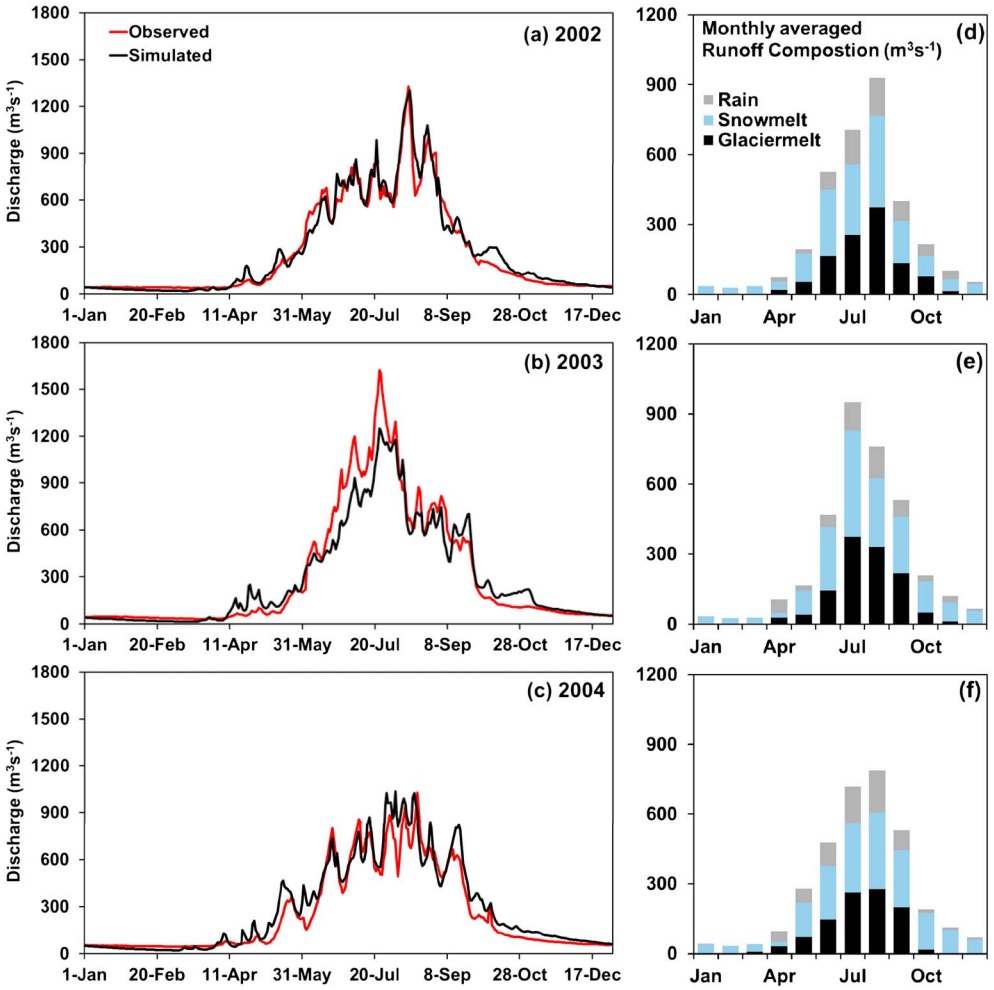

Figure 7. Comparison of simulated and observed discharge at Dainyor Bridge (Hunza River Basin outlet) in (a) 2002, (b) 2003, and (c) 2004; and model-simulated seasonal distribution of monthly average flow composition (rainfall, snowmelt, and glacier melt runoffs) in (d) 2002, (e) 2003, and (f) 2004.

the discharge peaked at ~1326 cumecs in mid-August, then dropped sharply to 630 cumecs within 1 week, and rose again as the glaciers received more energy to be melted out. Such a drastic reduction and an increase of discharge were well depicted by the model (see Figure 7a).

The validation years 2003 and 2004 had a different discharge regime than that in the calibration year 2002. Compared with observed discharge in the latter year, seasonal flows in 2003 increased substantially from the end of June through beginning of August. Peak flow was observed on 23 July, at 1621 cumecs. In 2004, there was considerable observed discharge in mid-May, followed by a decrease through 2 June. With the rise in temperature, the flow increased, following many downward and upward changes in association with temperature changes. Discharge in 2004 was less than that in 2002 and 2003. The model results tracked the observed discharge well in 2003, with NSE of 0.93 and coefficient of determination 0.97. However, the model overestimated discharge in early May and underestimated peak discharge significantly. RVE was

Table 6. Statistics and Flow Composition for Simulated Discharge in 2002–2004

Year	Rainfall Contribution	Snow Melt Contribution	Glacier Melt Contribution	NSE	RVE	R^2	Remarks
2002	16%	51%	33%	0.96	+0.03	0.98	Calibration
2003	16%	48%	36%	0.93	−0.06	0.97	Validation
2004	20%	49%	31%	0.90	+0.12	0.98	Validation

estimated at −0.06. In 2004, the model followed observations well, although there were some discrepancies in simulating the rise and fall of the hydrograph. The estimated NSE and RVE were 0.90 and +0.12, respectively. These discrepancies in discharge simulation were influenced by uncertainty in the meteorological input data, mainly the air temperature lapse rate (TLR) and precipitation. This is discussed in the following section.

An analysis of flow composition of the simulated discharge, i.e., snowmelt, glacier melt, and rainfall contributions to river discharge, is imperative for understanding the integrated hydrologic response of a catchment. These runoff components are presented here for the study area. Snowmelt runoff is that contributed by the sum of melting snow over land, clean, and debris-covered glaciers. Glacier melt runoff represents the melting of ice from both types of glaciers. Rainfall runoff is contributed by rainfall on land, snow, and glacier. Snowmelt runoff accounted for a large proportion of Hunza River runoff (about 50% for the 3 year average), whereas glacier melt runoff represented about 33%. Rainfall-induced runoff had the least contribution (17%). These figures did not vary much during the 3 year simulation (Table 5). In total, snow and glacier melt contributed about 83% to the river flow.

Figures 7d–7f represent monthly average runoff components from the model simulation. It was found that about 84% of runoff volume occurred in the summer melt season (May through September), whereas runoff was negligible during winter when most precipitation was stored as snow. Runoff from snow and glacier melt was mostly during April to November, with the peak in July to August. Winter runoff was mainly baseflow generated from snowmelt water that was stored in the soil. Snowmelt in April to June was related to snow accumulation during winter and spring. Snowmelt in summer (July to October) mainly originated from snowfall during that season. The glacier melt contribution was dominant in summer, mainly July to September. The peak varied in July to August, depending on air temperature and solar radiation.

5.3. Snow Cover Simulation

For evaluation of the model's capability to describe the seasonal evolution of snow cover, the simulated spatial distribution of snow cover was compared with that derived from MODIS. Figure 8a presents the simulated and MODIS-derived snow cover on selected dates of the calibration year (October 2001 through September 2002). In general, seasonal evolution of the spatial distribution of snow cover was in agreement with those inferred from the MODIS data; however, there were large discrepancies on some days. The model-simulated areal extent of snow cover tracked very well with that of MODIS. Snow covered about 80% of the basin from November through March, as predicted well by the model. This is because the model has strong correlation for events with fresh snowfall. With the increase of insolation and air temperature, the depletion of seasonal snow accelerates from mid-April, and the model follows the MODIS SCA except for remarkable overestimation after mid-June (Figure 8b). We believe that this overestimation is caused by misclassification of the pixels by MODIS for old snow and glaciers. Another reason for overestimation is possible classification of debris-covered glaciers as bare land by MODIS, whereas they are treated as SCA by the model. The simulated snow depletion pattern correlates well to the MODIS satellite data, with coefficient of correlation at 86% and average absolute bias at 6.27%. Seasonal averages of this bias are about 6% in October to December, 4.5% in January to March, 5.0% in April to June, and 9% in July to September.

A pixel-by-pixel comparison of simulated and MODIS SCAs was done for each 8 day period, and seasonality of evaluation indices is illustrated in Figure 8c. M_{AC} averaged over the entire year was 0.84, revealing its potential to predict snow and no-snow events, with ~84% accuracy. It is therefore concluded that the model is very likely (84% on average) to correctly predict snow cover if the MODIS snow cover product indicates snow, but when it does not, the model has a significant tendency (16% on average) to predict snow cover. The maximum and minimum M_{AC} for the study period was 0.94 and 0.76, respectively (Table 7). The minimum value was for the MODIS scene of 30 September 2002, owing to underestimation of snow cover from fresh snowfall. The M_{OE} and M_{UE} indices showed remarkable seasonality; however, these biases were less than 20%. Model overestimation is evident from mid-December to mid-February (winter season) and in June to August (summer). Winter bias is due to overestimation of snow cover at low elevation (Figure 8a), whereas summer bias is attributable to the failure of MODIS to map debris-covered and clean glaciers and old snow. It is well known that MODIS cannot differentiate snow and glaciers, and thus, it is very important that the model output identifies each grid as snow or glacier covered (clean ice or debris covered). Model underestimation is evident in March and April. This is because of uncertainty in the spatial distribution of snowfall, mainly in Khunjerab area (northeast part of the basin).

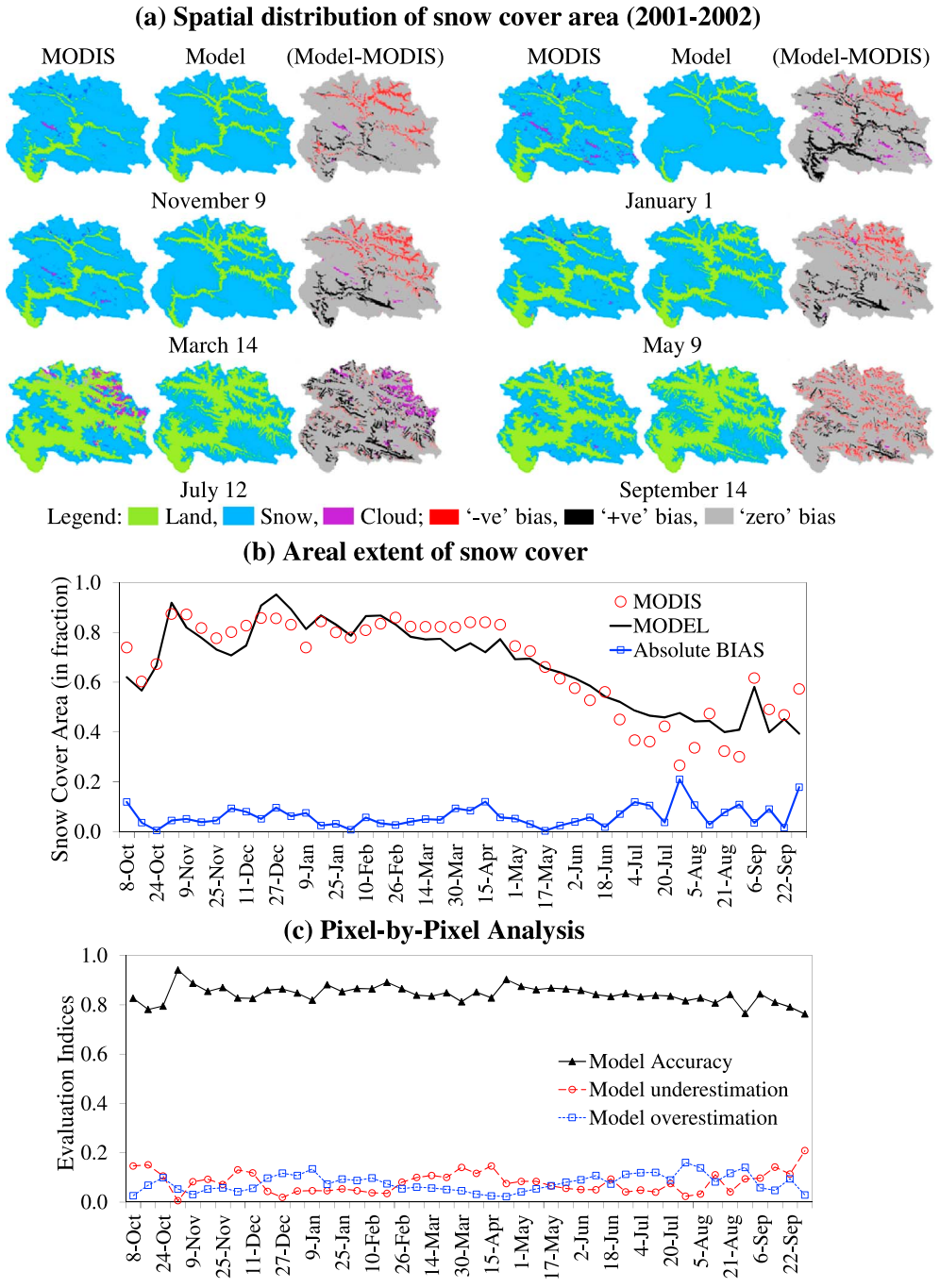

Figure 8. (a) Comparison for 2001–2002 of MODIS snow product (MOD10A2) and simulated snow-covered area, (b) areal extent of snow cover, and (c) evaluation indices.

Table 7. Statistics of Evaluation Indices for Snow Cover Simulation of 2002–2004

	Model Accuracy (M_{AC})			Model Overestimation (M_{OE})			Model Underestimation (M_{UE})		
Year	Max	Avg	Min	Max	Avg	Min	Max	Avg	Min
2002	0.942	0.843	0.763	0.160	0.076	0.022	0.208	0.080	0.005
2003	0.978	0.845	0.703	0.205	0.080	0.017	0.237	0.074	0.0
2004	0.963	0.854	0.716	0.149	0.070	0.013	0.261	0.076	0.009

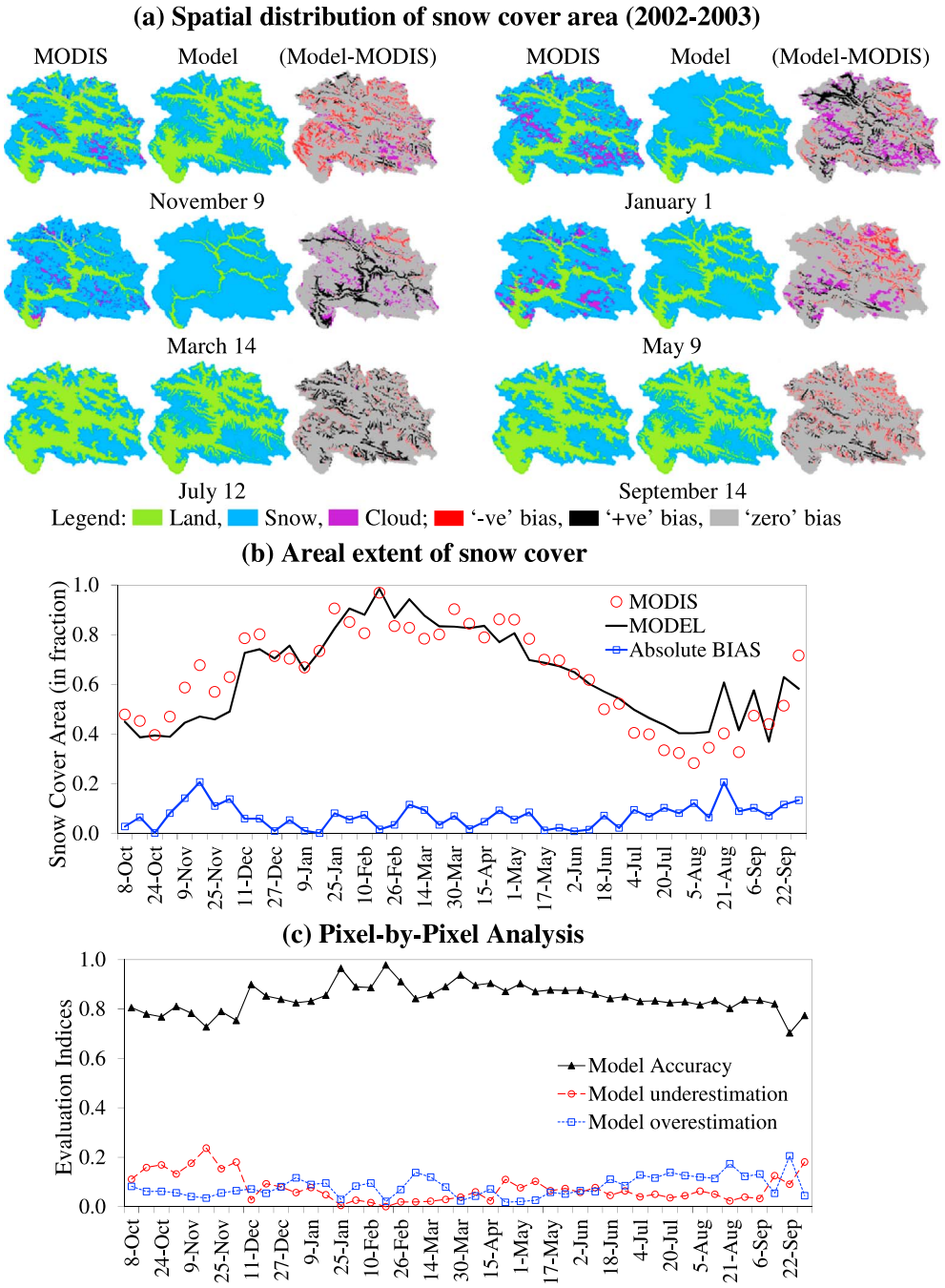

Figure 9. Same as Figure 8 but for 2002–2003.

The snow cover regime in 2002–2003 was different from that in 2001–2002 (Figure 9). The SCA was less than 80% until mid-December and maximized (95%) in mid-February because of heavy snowfall. Overestimation error became high afterward through the end of March, owing to model simulation of snow cover at low elevations. After March, the model tracked MODIS well but overestimated in summer following the results in 2001–2002 (Figure 9c). The overall correlation coefficient was about 84%, with average absolute bias 7%. The pixel-by-pixel analysis indicates average M_{AC}, M_{OE}, and M_{UE} at 0.84, 0.08, and 0.07, respectively (Table 7). However, the seasonal pattern indicates M_{OE} and M_{UE} ranges of 0.017–0.205 and 0.0–0.237, respectively. M_{AC} remained greater than 0.80 for all dates within the year, revealing good overall performance in simulating snow cover. In 2003–2004 (Figure 10), M_{AC}, M_{OE}, and M_{UE} were computed at

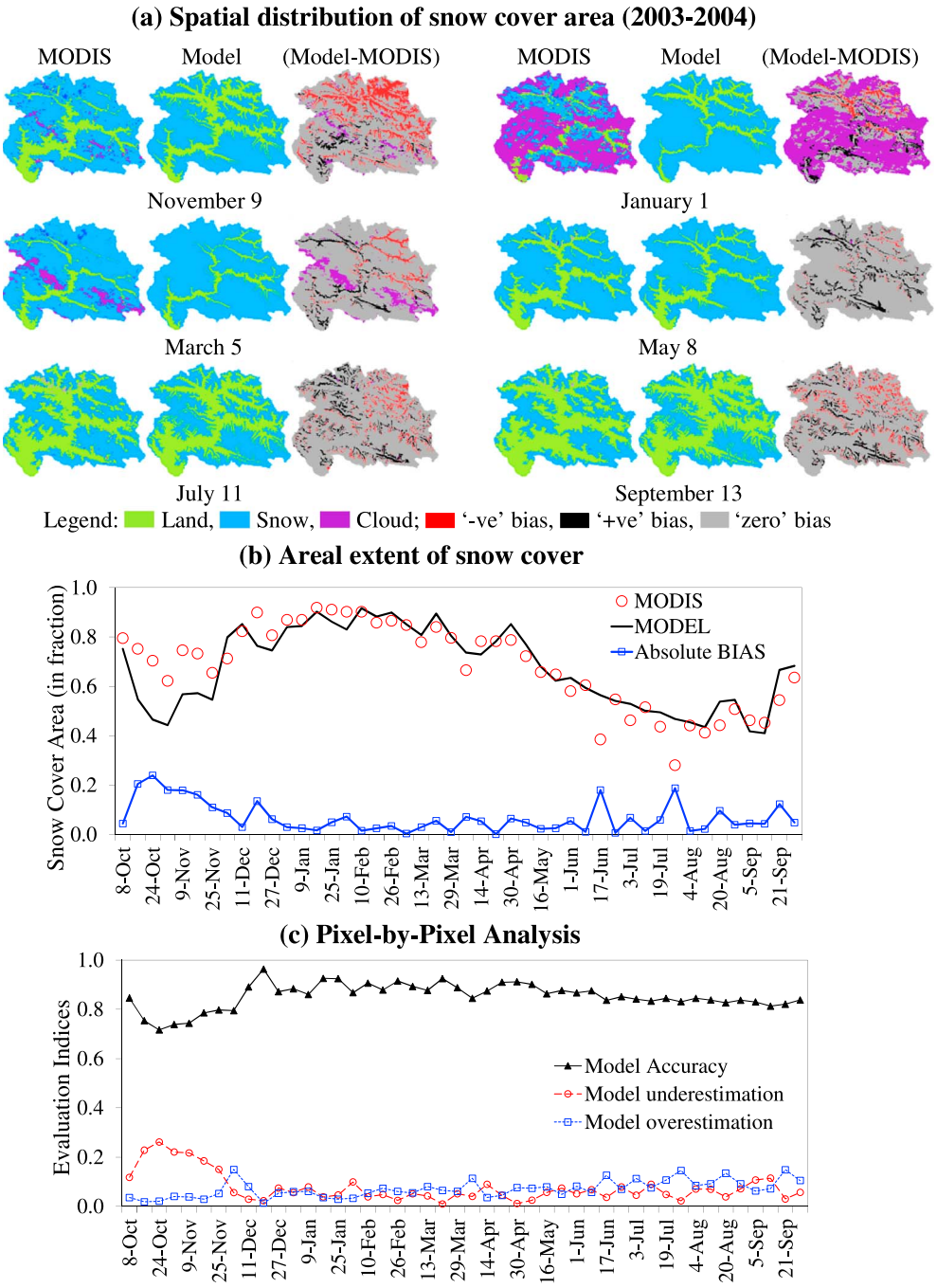

Figure 10. Same as Figure 8 but for 2003–2004.

0.85, 0.07, and 0.076, respectively (Table 7). The correlation between MODIS and the model simulations was 0.85, with average absolute bias 0.065. These evaluations give confidence for model performance in the spatial distribution of snow cover.

5.4. Snow/Glacier State Simulation

At each time step, the WEB-DHM-S model can simulate the state of snow or glaciers prognostically, in a spatially distributed manner. Here, maps of snow and glacier states for the 2001–2002 hydrologic year are discussed for highlighting the basic development and application of WEB-DHM-S. Initially, the model grids were assigned to snow and glacier states (snow-free land, snow-covered ground surface, clean glacier, and

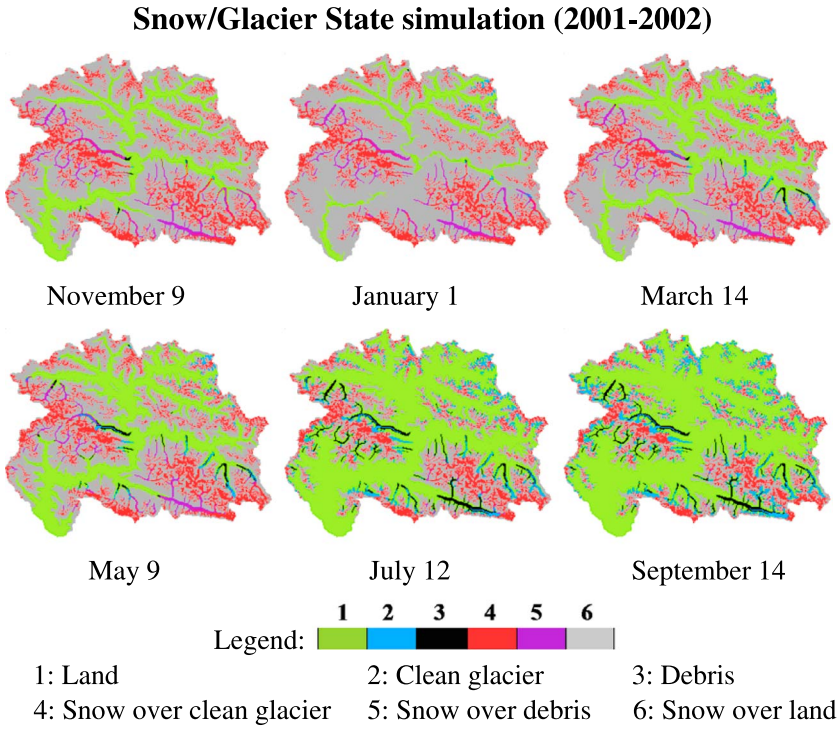

Figure 11. Spatial distribution of snow/glacier states in 2001–2002.

debris-covered glacier), based on a land cover map and glacier cover map from the ICIMOD [*Bajracharya and Shrestha*, 2011]. During simulation, these grids are updated prognostically following mass and energy balance for snow, land, and glaciers. It is essential to note that highly compacted snow is converted to ice based on density but that the model itself cannot simulate the evolution of debris over the glacier. Figure 11 shows that on 9 November, the majority of glaciers and land were covered with fresh snow. Low-elevation land and debris-covered glaciers were simulated as snow free. The maps for 1 January and 14 March show that all glaciers and some land were covered with new snow. Owing to the increase in temperature, this snow over low-lying ground surfaces began melting, which is seen in the maps of 9 May through 15 September. On 14 March, only 79.25 km^2 of ice was exposed to melt, with the transient snow line (TSL) at 2560 m altitude. About 79% of the basin was covered with fresh snow. By 9 May, the TSL had shifted 840 m upward to 3400 m, increasing the area of exposed glacier ice to 178 km^2. By 12 July, the TSL had risen to 4500 m, expanding the area of ice exposure to 727 km^2. A maximum TSL elevation of 5000 m was reached on 24 August, with 40% of the ice-covered portion of the basin exposed or a total 1100 km^2 of glacier ice. After completion of one full hydrologic year, the states at the end of September determine where the model grid gains mass (positive balance) or loses mass (negative mass), thereby achieving net annual mass balance.

5.5. Net Mass Balance Simulation

Mass balance measurements are difficult to make at large-scale river basins. Simulated results of net annual mass balance of the glaciers at this scale would be very informative in understanding the physical aspects of cryospheric processes. Average net mass balances (NMB) of major glaciers were determined and are shown in Figure 12 and Table 8. NMB was computed for the period 1 October to 30 September. Figure 12b indicates that melting was greatly high in 2002–2003 for all glaciers, resulting in a considerable overall negative NMB in Hunza River Basin. NMB in the basin was estimated at +0.132, −0.225, and +0.213 m yr^{-1} in 2001–2002, 2002–2003, and 2003–2004, respectively, with a 3 year mean of +0.04 m yr^{-1}. The latter value is in good agreement with other studies in the region. Previous modeling study of this basin [*Ragettli et al.*, 2013] revealed that total glacier mass was more or less constant during the simulation period 2001–2010 (+0.12 ± 0.1 m yr^{-1}). Analysis based on remote sensing and geodetic mass balance methods showed that glacier mass balance in the Karakoram during the early 21st century was relatively stable [*Gardelle et al.*, 2012,

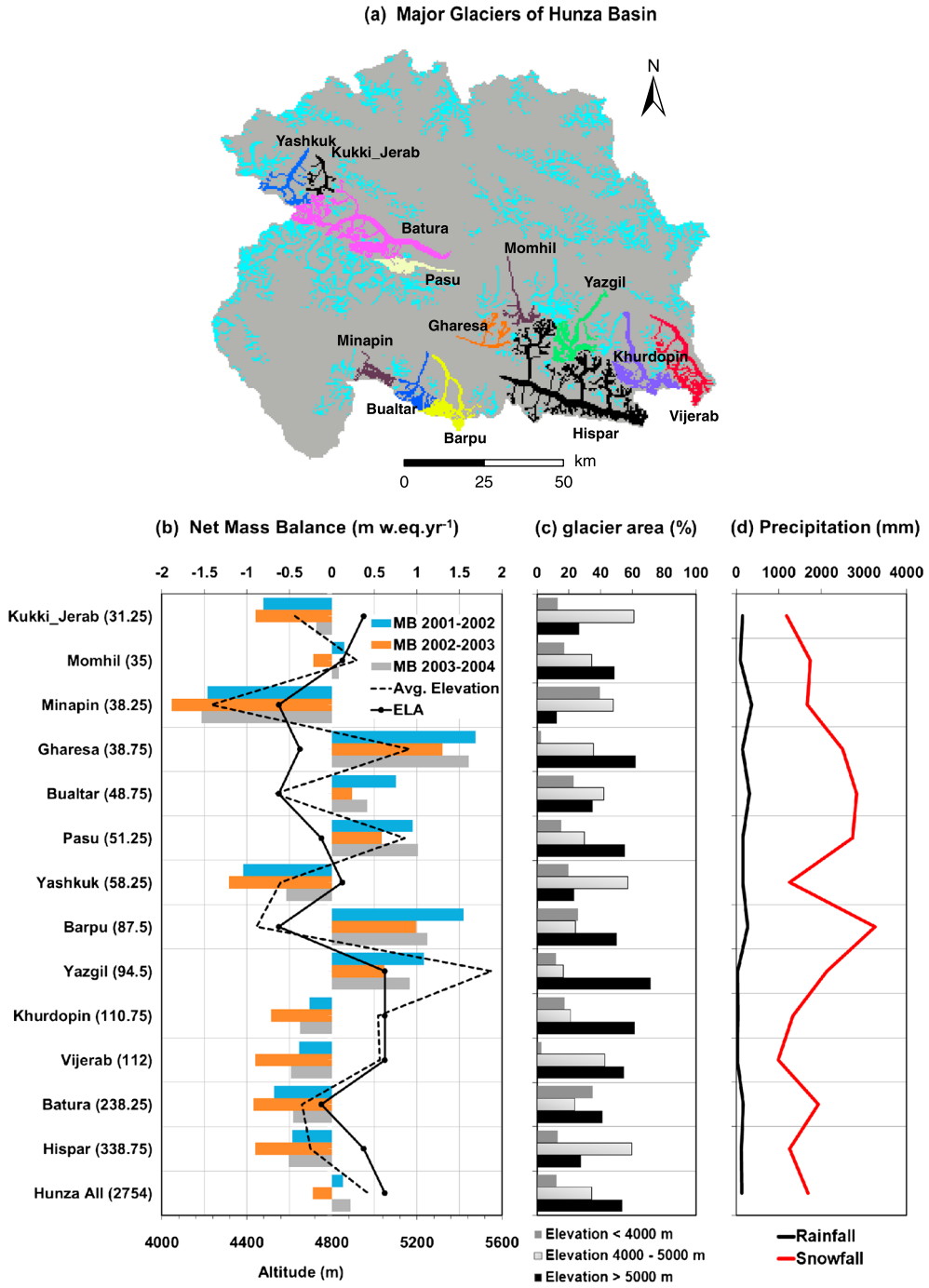

Figure 12. (a) Major glaciers of Hunza River Basin; (b) yearly net mass balance (NMB), average elevation of the glacier, and 3 year average equilibrium line altitude (ELA) for each glacier; (c) distribution of glacier area in percent within three elevation bands; (d) 3 year average snowfall and rainfall at each glacier.

2013; *Kääb et al.*, 2012; *Rankl et al.*, 2014]. The results of the present study were from a simulation of only 3 years; therefore, more modeling studies should be conducted for comparison on similar time frames.

NMB was positive at Yazgil, Gharesa, Bualtar, Pasu, and Barpu glaciers, and negative at Kukki Jerab, Minapin, Momhil, Yashkuk, Khurdopin, Vijerab, Batura, and Hispar glaciers. The equilibrium line altitude (ELA), where annual NMB becomes zero, is generally lower for greater snow accumulation. ELA and average elevation of each glacier are shown in Figure 12b. Areas of each glacier in three elevation zones (<4000 m,

Table 8. Simulated Accumulation (Acc; m yr^{-1}), Ablation (Abl; m yr^{-1}), Net Mass Balance (NMB; m yr^{-1}), and Equilibrium Line Altitude (ELA; m) for Glaciers of Hunza River Basin

Glacier Name	Area (km^2)	Average Elevation (m)	Area Above 5000 m (%)	2001–2002			2002–2003			2003–2004			3 year Avg. NMB	3 year Avg. ELA
				Acc.(+)	Abl.(−)	NMB	Acc.(+)	Abl.(−)	NMB	Acc.(+)	Abl.(−)	NMB		
Kukki_Jerab	31.25	4627	26.40	1.000	1.802	−0.802	1.168	2.065	−0.897	1.405	1.584	−0.179	−0.626	4950
Momhil	35.00	4917	48.57	1.815	1.672	+0.143	1.627	1.849	−0.222	1.793	1.713	+0.08	+0.000	4850
Minapin	38.25	4232	12.41	1.841	3.307	−1.466	1.549	3.434	−1.885	1.630	3.162	−1.532	−1.627	4550
Gharesa	38.75	5166	61.93	2.620	0.931	+1.690	2.342	1.042	+1.300	2.537	0.928	+1.609	+1.533	4650
Bualtar	48.75	4532	34.51	3.085	2.330	+0.755	2.636	2.401	+0.235	2.768	2.355	+0.413	+0.467	4550
Pasu	51.25	5143	55.12	2.740	1.791	+0.949	2.575	1.988	+0.587	2.880	1.868	+1.012	+0.849	4750
Yashkuk	58.25	4559	23.17	1.103	2.143	−1.04	1.217	2.428	−1.211	1.442	1.979	−0.537	−0.929	4850
Barpu	87.50	4446	48.47	3.556	2.007	+1.550	3.040	2.045	+0.995	3.197	2.073	+1.124	+1.223	4550
Yazgil	94.50	5550	71.42	2.240	1.156	+1.085	1.958	1.341	+0.617	2.186	1.271	+0.915	+0.872	5050
Khurdopin	110.75	5017	61.62	1.401	1.663	−0.262	1.225	1.942	−0.717	1.377	1.753	−0.376	−0.451	5050
Vijerab	112.0	5025	54.90	1.031	1.416	−0.385	0.904	1.806	−0.902	1.036	1.515	−0.479	−0.588	5050
Batura	238.25	4659	41.29	1.832	2.513	−0.680	1.836	2.756	−0.920	2.121	2.575	−0.454	−0.684	4750
Hispar	338.75	4700	27.60	1.316	1.779	−0.463	1.170	2.071	−0.901	1.275	1.781	−0.506	−0.623	4950
Hunza All	2754	4970	53.61	1.693	1.561	+0.132	1.587	1.812	−0.225	1.795	1.582	+0.213	+0.040	5050

4000–5000 m, and >5000 m) are presented in Figure 12c. Hypsography analysis for ELA indicated that the average ELA in Hunza River Basin was about 5050 m. However, ELA can vary by region and the type of the glacier nourishment, whether the glacier is accumulation fed or avalanche fed. Avalanche fed glaciers can further be categorized into the "Turkestan" and "Mustagh" types [*Hewitt*, 2014]. Snow and ice avalanches are predominant in Turkestan type where main ice streams start near the snow line with typically no accumulation zone. Ice streams start in the firn area of accumulation zone in Mustagh type glaciers. Typological categorization of major glaciers in Hunza basin can be found in *Hewitt* [2014]. The majority of the glaciers (such as Hispar, Batura, Vijerab, Khurdopin, Barpu, Pasu, Bualtar, and Gharesa) is Mustagh type where Minapin, Yashkuk, Momhil, and Kukki_Jerab glaciers are Turkestan type. ELA was at a relatively low altitude (4550 m) for Minapin Glacier, but the simulated NMB was strongly negative (about −1.46 to −1.88 m yr^{-1}). For the same ELA, Bualtar and Barpu glaciers had much larger positive mass balances (+0.235 to +0.755 m for Bualtar and +0.995 to +1.550 m for Barpu). The reason for large NMB variation for the same ELA is mainly topography effect. Average elevation of Minapin Glacier is very low, which means that there is a large contributing area at low elevation, ultimately affecting the distribution of precipitation (Figures 12c and 12d). Barpu and Bualtar glaciers have large percentages of glacier area at high elevation. However, simulated NMB was positive (+0.617 to +1.085 m) for Yazgil Glacier, which had a relatively high ELA (5050 m). This is mainly due to a relatively high average elevation, such that 70% of the glacier is above 5000 m. ELA was 5050 m for Vijerab glacier, with NMB from −0.385 to −0.902 m. Hispar and Batura make up the largest glacier system in Hunza River Basin, with glacier areas 338.75 and 238.25 km^2. NMB for Hispar in 2002 and 2004 was estimated at −0.463 m and −0.506 m, respectively, whereas it was −0.901 m in 2003. NMB for Batura Glacier was simulated at −0.680 m, −0.920 m, and −0.454 m for the 3 consecutive years. It is evident that NMB would be largely negative for Turkestan type glaciers as compared to Mustagh type glaciers since there is no or quite less accumulation region (e.g., Minapin and Yashkuk glaciers). Mustagh type glaciers showed mixed results for positive and negative NMB. From this analysis, it is concluded that the Hunza River Basin has strong spatial variation of glacier mass balance. Based on satellite data assessment, *Sarıkaya et al.* [2013] noted an increase of shrinking glaciers in the west and greater frequency of advancing glaciers in the east of Hindu Raj Basin, just west of Hunza River Basin. It is difficult to quantify spatial trends based on longitude. The present study yielded mixed results, irrespective of location, but were mainly dependent on glacier topography and the spatial distribution of precipitation. It is interesting that individual glaciers show similar characteristics of NMB over 3 years suggesting that both topography and glacier hypsometry play key roles in glacier mass balance.

5.6. Sensitivity Analysis

5.6.1. Sensitivity to Model Input

Although the model is well calibrated and validated as discussed in previous sections, it is prudent to investigate any consequences from potential uncertainties in model input, because inaccuracies of discharge, snow cover,

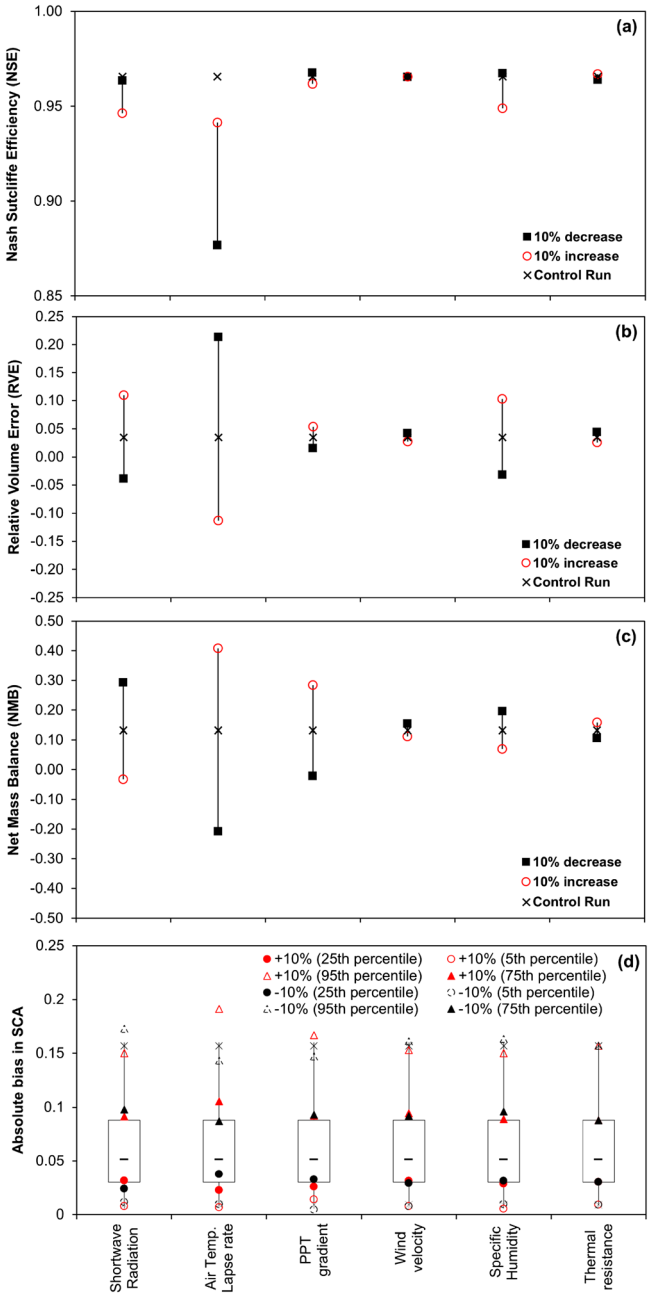

Figure 13. Model sensitivity to ±10% variation of input data in terms of (a) Nash-Sutcliffe efficiency, (b) relative volume error, (c) net mass balance, and (d) box plot of absolute bias in SCA. Horizontal line within each box represents 50th percentile, the top (bottom) line of the box the 75th (25th) percentile, and the end of the top (bottom) line with whiskers the 95th (5th) percentile.

and glacier mass balance simulations are strongly influenced by meteorological input data. The scarcity of meteorological stations in the study area is the major limitation for hydrologic modeling. However, several simulation experiments were designed for a prescribed range of variation (±10%) of model input (TLR, shortwave radiation, wind speed, specific humidity, and precipitation gradient). This analysis was performed for the calibration year 2001–2002. Because a majority of the land cover is snow/ice and bare soil, sensitivity to variations of LAI/FPAR were not assessed. Discharge evaluation indices for snow cover and NMB were explored for each experiment.

It was speculated that both increased and decreased shortwave radiation significantly alter the RVE (+10% change produces +0.11 RVE and −10% yields −0.04), but the impacts on NSE are insignificant. The 95th percentile of absolute bias for SCA increased in both experiments. Increased shortwave radiation enhanced glacier melt and vice versa, resulting in NMB of −0.03 m (+10%) and +0.29 m (−10%) (see Figure 13). In order to have an idea of impact of shortwave radiation, the simulation with raw GLDAS (without correction) was also carried out. A large negative bias in SCA in April and May was speculated due to early melt of snow, which led to early exposure of glaciers. Consequently, glacier melt increased, causing NMB at −0.93 m, NSE at 0.52 and RVE at +0.49. For increased TLR, both snow and glacier melt decreased, resulting in significant underestimation of discharge (RVE at −0.11; NSE at 0.941) and positive NMB (+0.40 m). A decreased TLR shows the opposite situation as expected, with greater negative NMB (−0.20 m) and strong discharge overestimation, with RVE at +0.21 and NSE at 0.88. There was strong variation in absolute bias of SCA (25th, 75th, and 90th percentiles) for both ± variation of TLR. An increased precipitation gradient augmented the amount of snowfall, which ultimately enhanced the positive NMB; it had less effect on discharge and SCA simulation. Alteration of specific humidity controls latent heat flux, which affects the surface energy balance to some extent. RVE and NMB had significant changes, but NSE and bias of SCA did not vary remarkably with respect to the control run. Wind speed showed the least influence among model inputs. Variations of thermal resistance

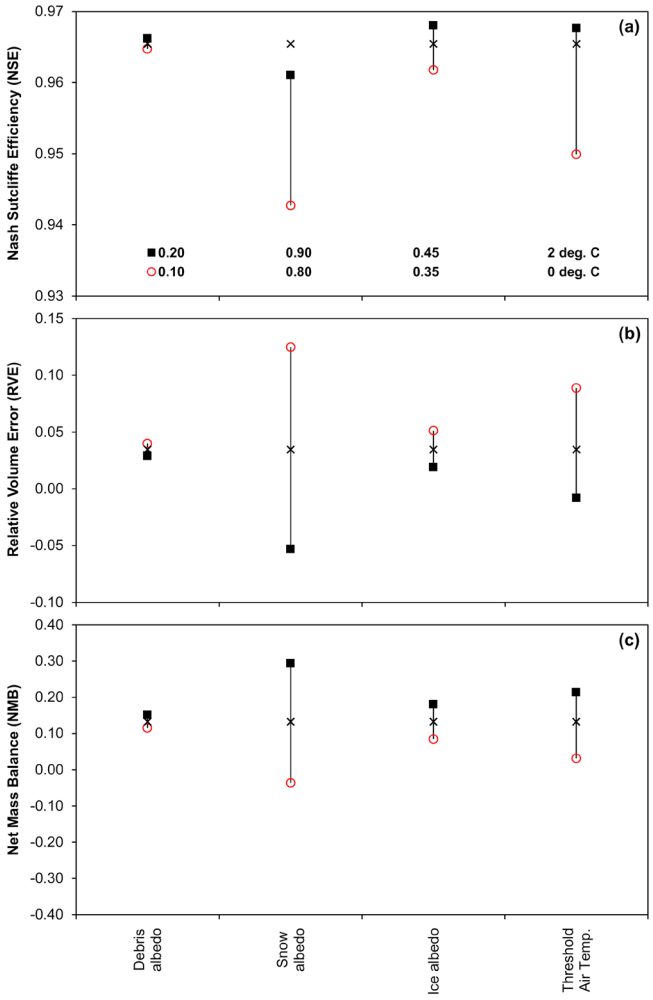

Figure 14. Model sensitivity to parameters, debris thermal resistance, ice albedo, debris albedo, and threshold air temperature in terms of (a) Nash-Sutcliffe efficiency, (b) relative volume error, and (c) net mass balance. Model sensitivity was not significant in terms of absolute bias in SCA.

had insignificant impacts on simulation results. From this analysis, we conclude that the order of model sensitivity is TLR, shortwave radiation, precipitation gradient, specific humidity, and wind speed.

5.6.2. Sensitivity to Model Parameters

Additionally, model sensitivity versus major model parameters was addressed. Simulation runs were executed for debris albedos 0.10 and 0.20, fresh snow albedos 0.80 and 0.90, ice albedos 0.35 and 0.45, and threshold air temperatures (T_{th}, designating snow/rain separation) 0 and 2 °C. Because debris albedo governs NMB of debris-covered glaciers only, its effect on discharge, SCA, and overall NMB is negligible. With decrease/increase of snow albedo, snowmelt was enhanced/retarded, which influences model results significantly. NMB varied from −0.03 to +0.3 m and RVE from +0.12 to −0.05 for decrease-increase simulation, but NSE was still greater than 0.94. Reduction of ice albedo means an increase in absorption of shortwave radiation, causing greater ice melt. RVE deteriorated to +0.124 with a decreased positive NMB (+0.084 m). Increase of ice albedo reduced available energy and increased positive NMB (+0.179 m). Increase of T_{th} accelerated the tendency to increase snowfall, resulting in greater positive NMB. RVE degraded significantly when T_{th} was increased from 0 to 2 °C, although NSE was 0.95–0.97 (Figure 14). This sensitivity analysis showed that improvement of one efficiency criterion may reduce the other criteria; individual efficiency criteria in the experiments varied considerably.

5.6.3. Sensitivity to Change in Glacier Extent

The majority of the glaciers in this basin has their thickness above 100 m. Thus, there is less chance of reduction of glacier extent. However, the hypothetical glacier extent is prepared by not considering the glaciers with 50 m thickness that renders reduction of 18% in clean glaciers from current extent. Figure 15 presents the sensitivity of discharge to change in glacier extent. It is found that the sensitivity of streamflow to glacier area changes is remarkably small and within the error band associated with uncertainty in model input and model parameters (see Figure 15). The reduction in glacier melt contribution was 1% in 2002, whereas this value was 1.4% in 2003 and 1.1% in 2004.

5.6.4. Seasonal Sensitivity

Seasonal sensitivity characteristics (SSC) was obtained by perturbing air temperature and precipitation in each month separately following the concept of *Oerlemans and Reichert* [2000]. These sensitivities $C_{T,k}$ and $C_{P,k}$ are defined as $\partial v/\partial T$ and $\partial v/\partial P$, respectively, where v is a variable (NMB or Runoff). Therefore, $C_{T,k}$ is the change in NMB or Runoff for temperature perturbations of 1 K in month k, and $C_{P,k}$ is the

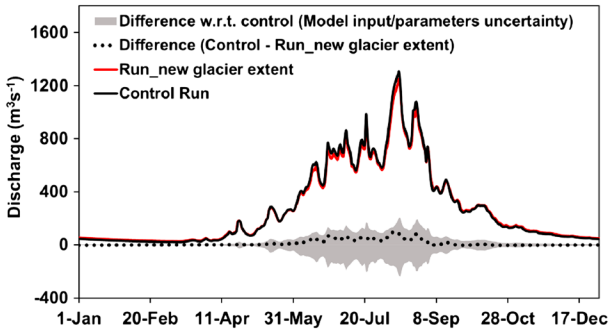

Figure 15. Model sensitivity to change in glacier extent in 2002.

change in NMB or runoff for precipitation perturbations of 10%. Figure 16 shows the SSC ($C_{T,k}$ and $C_{P,k}$) in relation to the NMB. During November to March, large proportion of precipitation falls as snow and insignificant melting occurs, so temperature perturbations in these months show less sensitivity where it shows higher sensitivity in June to August. It is interesting to note that precipitation is considerably important throughout the year with large effects on December, February, and April. This is because the ratio of snowfall to total precipitation is significantly increased. The SSC in relation to monthly runoff in four months (June to September) are illustrated in Figure 17. It is evident that $C_{T,k}$ and $C_{P,k}$ in month k would have higher sensitiveness in the corresponding month. But it is worthy to note that the air temperature perturbations ($C_{T,k}$) in previous month has significant effect in the runoff of month k. On the contrary, it is found that precipitation perturbations in winter and spring months show considerable impacts on runoff. Perturbation in August had a larger sensitivity of $C_{T,k}$ and $C_{P,k}$ because significant snow and glacier melt occurs in this month, along with monsoon fed precipitation. Therefore, increased precipitation with warming climate would increase the probability of occurence of a devastating flood in this basin.

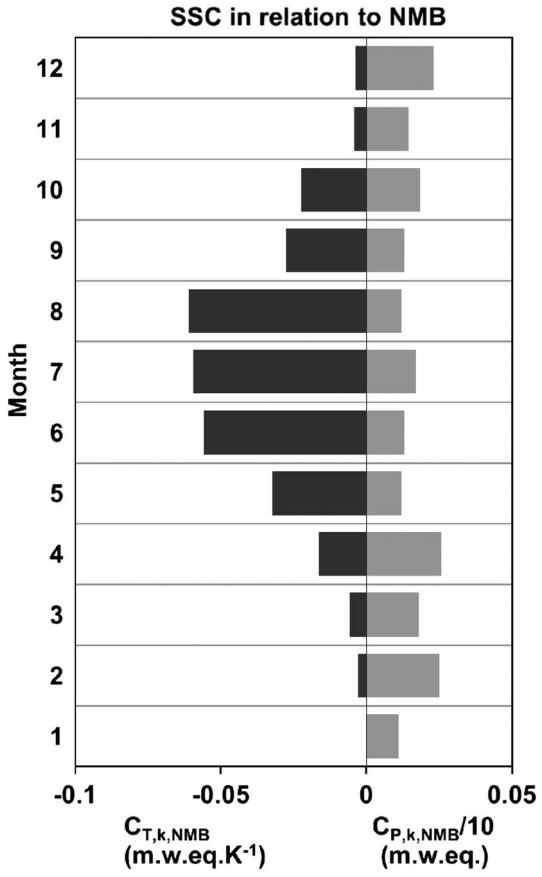

Figure 16. Seasonal sensitivity characteristics (SSC) for Hunza basin in relation to NMB in 2002.

5.7. Model Limitations

A number of limitations have been recognized in our model formulation that could be addressed in the future to enhance its wide applicability. For example, glacier dynamics is not included in this study. Although exclusion of glacier dynamics will not affect short-term simulations, it will have a large impact for the long-term simulation and the results for changes in glacier extent might be biased. Consequently, this bias will affect streamflow simulation. Moreover, the uncertainty in initial ice thickness may impose biases in the simulated glacier extent, NMB, and streamflow; however, the biases are insignificant for the short-term simulation. Inclusion of glacier dynamics will resolve the issue of ice thickness as the glacier dynamics model could be run prior in time for 1000 years to get the initial condition of ice thickness and glacier extent, as discussed by *Naz et al.* [2014]. The assumption of a constant albedo for clean and debris-covered glacier is another limitation of this modeling framework as it is shown that the model is sensitive to glacier albedo. Future work should be

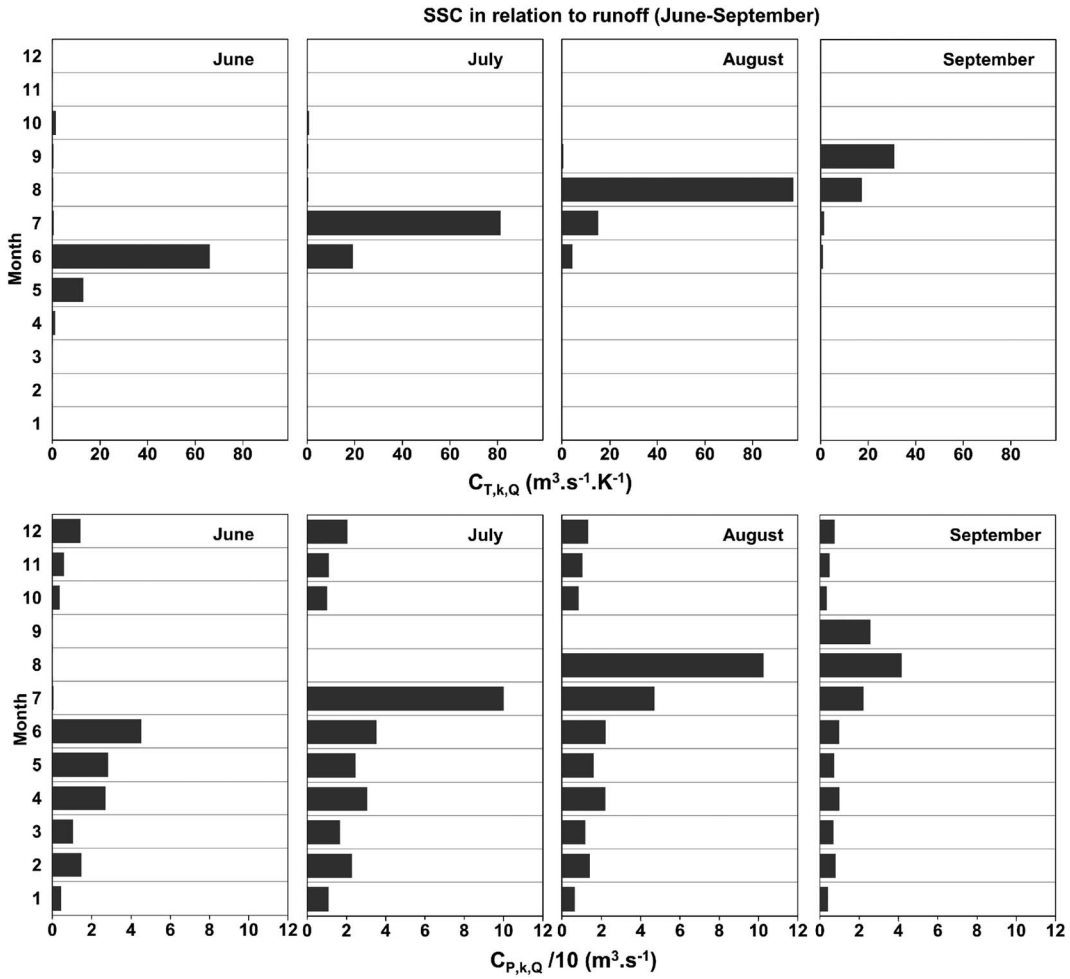

Figure 17. SSC in relation to runoff (June to September) in 2002. Upper tier shows the sensitivity to monthly air temperature perturbations ($C_{T,k}$), and lower tier shows the sensitivity to monthly precipitation perturbations ($C_{P,k}$).

conducted to formulate time variant albedo over glacier surfaces by using the albedo from satellite imagery and in situ measurements.

6. Conclusions

This study presented integration of an energy balance-based glacier model (clean and debris covered) with an advanced, multilayer, energy balance-based snowmelt model within a distributed hydrologic modeling framework (WEB-DHM-S). This was done to enhance existing SSVAT-based distributed hydrologic modeling, resulting in improved model performance for a cold mountain catchment. The integrated system was applied to the Hunza River basin in the Karakoram region of Pakistan, where snow and glacier melt runoff is the major contributor to river discharge. A thorough evaluation of the model against river discharge and MODIS snow cover was done, providing valuable information on flow composition of the river discharge, NMB, ELA, and model sensitivity to uncertainty in its input and parameters.

The results demonstrate that the model is able to reproduce the river discharge satisfactorily, with NSE of 0.96 and RVE of +0.03 in the calibration year 2002. During validation years 2003 and 2004, a remarkable negative (−0.06) and positive (+0.12) bias of discharge was simulated, despite satisfactory NSEs of 0.93 and 0.90, respectively. We presented an analysis of flow composition of the simulated river discharge, i.e., snowmelt, glacier melt, and rainfall contributions to that discharge. Snowmelt runoff accounted for a large proportion of Hunza River runoff (about 50% for 3 year average), whereas glacier melt runoff contributed about 33%. Rainfall-induced runoff had the smallest contribution (17%). Interannual variation

of these contributions did not vary significantly. In total, snow and glacier melt contributed about 83% to the river flow. Evaluation of the simulated spatial distribution of SCA versus a MODIS snow cover product indicated that the areal extent of snow cover was reproduced well, with average absolute bias 6.5% and coefficient of correlation about 86%. Bias on certain dates was large, owing to a failure to represent the spatial variability of precipitation. Evaluation indices derived from qualitative pixel-to-pixel analysis between the model and MODIS-derived SCA illustrated that the model is capable of predicting snow events with average accuracy 84%.

In addition, model capability of prognostically simulating the state of snow and glaciers at each model grid was demonstrated, providing important information for understanding the variation of the TSL in such a remote basin. NMB in the Hunza River Basin was estimated at +0.132, −0.225, and +0.213 m yr^{-1} in 2001–2002, 2002–2003, and 2003–2004, respectively, with a 3 year mean at +0.04 m yr^{-1}. NMB analysis for 13 individual glaciers indicated that it was positive at Yazgil, Momhil, Gharesa, Bualtar, Pasu, and Barpu glaciers, and negative at Kukki Jerab, Minapin, Yashkuk, Khurdopin, Vijerab, Batura, and Hispar glaciers. Hypsographic analysis for ELA suggests that its average in the Hunza River Basin is about 5050 m. Glaciers with the same ELA have large NMB variations because of the effect of topography. As topography and glacier hypsometry both play key role in NMB simulation, it is found that glaciers with positive or negative NMB attain similar characteristics over 3 years.

The study region has a scarcity of meteorological stations. Given this major limitation, there were uncertainties in the present study regarding the distribution of model input data and simulations. We investigated the impacts of uncertainty (±10% variation relative to the default control run) in such input and parameters in the simulation of discharge, SCA and NMB. This revealed air temperature as the model data input that produced the greatest variation of model simulation results. Model sensitivity to shortwave radiation input data was also significant, relative to wind speed and humidity. Although variation of thermal resistance, debris and ice albedo, and snow/rain threshold temperature had significant effects on mass balance simulation, their impacts on discharge and SCA were not significant. Seasonal sensitivity analysis revealed that precipitation changes are important throughout the year where air temperature show its sensitivity in summer period only. Through such evaluations, WEB-DHM-S demonstrated its capacity to satisfactorily address basin-scale snow and glacier processes in the Hunza River Basin. Further investigations of the spatial distribution of station temperature data on the catchment grid are required for additional improvements to model simulations. To this end, this study was the first to adopt a SSVAT-based distributed hydrologic model with a physically based, multilayer snow and glacier module to estimate the spatial distribution of snow cover and snow and glacier melt runoff in the Karakoram region. The main limitation of this study is the lacking of glacier dynamics; thus, this modeling system could not be applicable for long-term simulations and could not be able to address changes in glacier extent which will certainly affect streamflow simulation. In future work, glacier dynamics will be integrated in the current modeling system for long-term simulation, so that changes in glacier extent can be accurately predicted and the impact of climate change on similar snow- and glacier-dominated river basins can be adequately addressed. Furthermore, application of the model to such basins with different climates is essential for improving and validating the modeling system.

Author Contributions

M.S. led the development of this study, developed hydrologic model, carried out all simulation and analysis and led the writing of this manuscript. T.K., Y.H., Y.X., and L.W. contributed to the development of the snow and glaciermelt model and the writing. G.R. and B.A. contributed to the management of the data set, analysis, and the writing.

Acknowledgments

This study was supported by grants from the Ministry of Education, Culture, Sports, Science and Technology of Japan. The first author is supported by Water and Energy Commission Secretariat (WECS), Government of Nepal. Land cover data were downloaded from http://edc2.usgs.gov/glcc/glcc.php. SRTM digital elevation data were downloaded from http://srtm.csi.cgiar.org/. Glacier cover inventory data for Hunza basin were furnished by ICIMOD. Soil parameter data were from FAO. Surface meteorological data and river discharge data were provided by Water and Power Development Authority of Pakistan (WAPDA). GLDAS data products, MOD10A2 snow cover products, and MOD15A2 LAI and FPAR products were provided by the National Aeronautics and Space Administration (NASA) Earth Observing System Data and Information System (http://reverb.echo.nasa.gov). APHRODITE precipitation data sets were downloaded from http://www.chikyu.ac.jp/precip/. The authors are supported by the Data Integration and Analysis System for providing the data integration resources. The authors are highly indebted to anonymous reviewers whose comments and suggestions have significantly improved the quality of the manuscript.

References

Ageta, Y., N. Naito, M. Nakawo, K. Fujita, K. Shankar, A. P. Pokhrel, and D. Wangda (2001), Study project on the recent rapid shrinkage of summer-accumulation type glaciers in the Himalayas, 1997–1999, *Bull. Glaciol. Res.*, *18*, 45–49.

Akhtar, M., N. Ahmad, and M. J. Booij (2008), The impact of climate change on the water resource of Hindukush-Karakorum-Himalaya region under different glacier coverage scenarios, *J. Hydrol.*, *355*, 148–163.

Anslow, F. S., S. Hostetler, W. R. Bidlake, and P. U. Clark (2008), Distributed energy balance modeling of South Cascade Glacier, Washington and assessment of model uncertainty, *J. Geophys. Res.*, *113*, F02019, doi:10.1029/2007JF000850.

Archer, D. R. (2003), Contrasting hydrological regimes in the upper Indus Basin, *J. Hydrol.*, *274*, 198–210.

Archer, D. R., and H. J. Fowler (2004), Spatial and temporal variations in precipitation in the upper Indus Basin, global teleconnections and hydrological implications, *Hydrol. Earth Syst. Sci.*, *8*, 47–61.
Bajracharya, S. R., and B. Shrestha (2011), *The Status of Glaciers in the Hindu Kush-Himalayan Region*, 127 pp., ICIMOD, Kathmandu.
Barnett, T. P., J. C. Adam, and D. P. Lettenmaier (2005), Potential impacts of a warming climate on water availability in snow-dominated regions, *Nature*, *438*, 303–309.
Benn, D. I., T. Bolch, K. Hands, J. Gulley, A. Luckman, L. I. Nicholson, D. Quincey, S. Thompson, R. Toumi, and S. Wiseman (2012), Response of debris-covered glaciers in the Mount Everest region to recent warming, and implications for outburst flood hazards, *Earth Sci. Rev.*, *114*(1–2), 156–174.
Bolch, T., et al. (2012), The state and fate of Himalayan Glaciers, *Science*, *336*, 310–314, doi:10.1126/science.1215828.
Bookhagen, B., and D. W. Burbank (2010), Toward a complete Himalayan hydrological budget: Spatiotemporal distribution of snowmelt and rainfall and their impact on river discharge, *J. Geophys. Res.*, *115*, F03019, doi:10.1029/2009JF001426.
Braun, L. N., W. Grabs, and B. Rana (1993), Application of a conceptual precipitation-runoff model in the Langtang Khola basin, Nepal Himalaya, in *Snow and Glacier Hydrology*, vol. 218, edited by G. J. Young, pp. 221–237, IAHS.
Brock, B. W., I. C. Willis, M. J. Sharp, and N. S. Arnold (2000), Modelling seasonal and spatial variations in the surface energy balance of Haut Glacier d'Arolla, Switzerland, *Ann. Glaciol.*, *31*, 53–62.
Cazorzi, F., and G. D. Fontana (1996), Snowmelt modeling by combining air temperature and a distributed radiation index, *J. Hydrol.*, *181*, 169–187.
Cherkauer, K. A., and D. P. Lettenmaier (2003), Simulation of spatial variability in snow and frozen soil, *J. Geophys. Res.*, *108*(D22), 8858, doi:10.1029/2003JD003575.
Cogley, J. G. (2011), Himalayan glaciers in 2010 and 2035, in *Encyclopedia of Snow, Ice and Glaciers*, edited by V. P. Singh, P. Singh, and U. K. Haritashya, pp. 520–523, Springer, Berlin.
Crawford, T. M., and C. E. Duchon (1999), An improved parameterization for estimating effective atmospheric emissivity for use in calculating daytime downwelling longwave radiation, *J. Appl. Meteorol.*, *38*, 474–480.
Decker, M., M. A. Brunke, Z. Wang, K. Sakaguchi, X. Zeng, and M. G. Bosilovich (2012), Evaluation of the reanalysis products from GSFC, NCEP, and ECMWF using flux tower observations, *J. Clim.*, *25*, 1916–1944.
Dickinson, R. E., A. Henderson-Sellers, and P. J. Kennedy (1993), Biosphere–Atmosphere Transfer Scheme (BATS) Version 1e as coupled to the NCAR Community Climate Model, *NCAR Tech. Note TN-387 1 STR*, 72 pp.
Duan, Q., S. Sorooshian, and V. Gupta (1992), Effective and efficient global optimization for conceptual rainfall-runoff models, *Water Resour. Res.*, *28*(4), 1015–1031, doi:10.1029/91WR02985.
Dyurgerov, M. B., and M. F. Meier (2004), *Glaciers and the Changing Earth System: A 2004 Snapshot*, *Occas. Pap.*, vol. 58, 117 pp., Institute of Arctic and Alpine Research, Boulder, Colo.
FAO (2003), Digital soil map of the world and derived soil properties, Land and Water Digital Media Series Rev. 1, United Nations Food and Agriculture Organization, available in CR-ROM.
Fassnacht, S. R., and E. D. Soulis (2002), Implications during transitional periods of improvements to the snow processes in the land surface scheme-hydrological model WATCLASS, *Atmos. Ocean*, *40*, 389–403.
Fowler, H. J., and D. R. Archer (2006), Conflicting signals of climate change in the upper Indus Basin, *J. Clim.*, *19*, 4276–4292.
Gardelle, J., E. Berthier, and Y. Arnaud (2012), Slight mass gain of Karakoram glaciers in the early twenty-first century, *Nat. Geosci.*, *5*, 322–325, doi:10.1038/NGEO1450.
Gardelle, J., E. Berthier, Y. Arnaud, and A. Kääb (2013), Region-wide glacier mass balances over the Pamir-Karakoram-Himalaya during 1999–2011, *Cryosphere*, *7*, 1263–1286, doi:10.5194/tc-7-1263-2013.
Garen, D. C., and D. Marks (2005), Spatially distributed energy balance snowmelt modeling in a mountainous river basin: estimation of meteorological inputs and verification of model results, *J. Hydrol.*, *315*, 126–153.
Gurtz, J., A. Baltensweiler, and H. Lang (1999), Spatially distributed hydrotope-based modelling of evapotranspiration and runoff in mountainous basins, *Hydrol. Processes*, *13*, 2751–2768.
Hewitt, K. (2005), The Karakoram anomaly? Glacier expansion and the "elevation effect", Karakoram Himalaya, *Mt. Res. Dev.*, *25*, 332–340.
Hewitt, K. (2014), *Glaciers of the Karakoram Himalaya, Glacial Environments, Processes, Hazards and Resources*, 363 pp., Springer, Dordrecht, Netherlands.
Hewitt, K., C. P. Wake, G. J. Young, and C. David (1989), Hydrological investigation at Biafo Glacier, Karakoram range, Himalaya: An important source of water for the Indus river, *Ann. Glaciol.*, *13*, 103–108.
Hock, R. (1999), A distributed temperature-index ice- and snowmelt model including potential direct radiation, *J. Glaciol.*, *45*(149), 101–111.
Hock, R. (2005), Glacier melt: A review of precesses and their modeling, *Prog. Phys. Geogr.*, *29*(3), 362–391.
Hock, R., and B. Holmgren (2005), A distributed energy balance model for complex topography and its application to Storglaciären, Sweden, *J. Glaciol.*, *51*(172), 25–36.
Immerzeel, W. W., P. Droogers, S. M. de Jong, and M. F. P. Bierkens (2009), Large-scale monitoring of snow cover and runoff simulation in Himalayan river basins using remote sensing, *Remote Sens. Environ.*, *113*, 40–49.
Immerzeel, W. W., L. P. H. van Beek, and M. F. P. Bierkens (2010), Climate change will affect the Asian water towers, *Science*, *328*(5984), 1382–1385.
Immerzeel, W. W., L. P. H. van Beek, M. Konz, A. B. Shrestha, and M. F. P. Bierkens (2012a), Hydrological response to climate change in a glacierized catchment in the Himalayas, *Clim. Change*, *110*, 721–736, doi:10.1007/s10584-011-0143-4.
Immerzeel, W. W., F. Pellicciotti, and A. B. Shrestha (2012b), Glaciers as a proxy to quantify the spatial distribution of precipitation in the Hunza basin, *Mt. Res. Dev.*, *32*(1), 30–38.
Immerzeel, W. W., F. Pellicciotti, and M. F. P. Bierkens (2013), Rising river flows throughout the twenty-first century in two Himalayan glacierized watersheds, *Nat. Geosci.*, doi:10.1038/ngeo1896.
Jordan, R. (1991), A one-dimensional temperature model for a snow cover, U.S. Army Corps of Engineers, Cold Regions Research and Engineering Laboratory, Special Rep. 91–16, pp. 49.
Kääb, A., E. Berthier, C. Nuth, J. Gardelle, and Y. Arnaud (2012), Contrasting patterns of early 21st century glacier mass change in the Himalayas, *Nature*, *488*, 495–498, doi:10.1038/nature11324.
Kayastha, R. B., Y. Ageta, and K. Fujita (2005), Use of positive degree day methods for calculating snow and ice melting and discharge in glacierized basins in the Langtang valley, Central Nepal, in *Climate and Hydrology in Mountain Areas*, edited by C. D. Jong, pp. 7–14.
Klein, A. G., and A. C. Barnett (2003), Validation of daily MODIS snow cover maps of the Upper Rio Grande River Basin for the 2000–2001 snow year, *Remote Sens. Environ.*, *86*, 162–176.
Klok, E. J., and J. Oerlemans (2002), Model study of the spatial distribution of the energy and mass balance of Morteratschgletscher, Switzerland, *J. Glaciol.*, *48*(163), 505–518.

Konz, M., S. Uhlenbrook, L. Braun, A. Shrestha, and S. Demuth (2007), Implementation of a process based catchment model in a poorly gauged, highly glacierized Himalayan headwater, *Hydrol. Earth. Syst. Sci.*, *11*, 1323–1339.
Kotlarski, S., D. Jacob, R. Podzun, and F. Paul (2010), Representing glaciers in a regional climate model, *Clim. Dyn.*, *34*, 27–46.
Kouwen, N., E. D. Soulis, A. Pietroniro, J. Donald, and R. A. Harrington (1993), Grouping response units for distributed hydrologic modelling, *J. Water Resour. Plann. Manag.*, *119*(3), 289–305.
Lemke, P., et al. (2007), Observations: Changes in snow, Ice and frozen ground, in *Climate Change 2007: The Physical Science Basis. Contribution of Working Group I to the Fourth Assessment Report of the Intergovernmental Panel on Climate Change*, Cambridge Univ. Press, Cambridge, U. K., and New York.
Li, X. G., and M. W. Williams (2008), Snowmelt runoff modeling in an arid mountain watershed, Tarim Basin, China, *Hydrol. Processes*, *22*, 3931–3940.
Liang, X., D. P. Lettenmaier, E. Wood, and S. J. Burges (1994), A simple hydrologically based model of land surface water and energy fluxes for GSMs, *J. Geophys. Res.*, *99*(D7), 14,415–14,428, doi:10.1029/94JD00483.
Lowe, A. T., and D. N. Collins (2000), Modelling runoff from large glacierized basins in the Karakoram Himalaya using remote sensing of the transient snowline, in *Remote Sensing and Hydrology*, vol. 267, edited by M. Owe et al., pp. 99–104, IAHS.
Luo, Y., J. Arnold, S. Liu, X. Wang, and X. Chen (2013), Inclusion of glacier processes for distributed hydrological modeling at basin scale with application to a watershed in Tianshan Mountains, northwest China, *J. Hydrol.*, *477*, 72–85.
Machguth, H., F. Paul, M. Hoelzle, and W. Haeberli (2006), Distributed glacier mass balance modeling as an important component of modern multi-level glacier monitoring, *Ann. Glaciol.*, *43*, 335–343.
Mayer, C., A. Lambrecht, C. Mihalcea, M. Belò, G. Diolaiuti, C. Smiraglia, and F. Bashir (2010), Analysis of glacial meltwater in Bagrot Valley, Karakoram: Based on short-term ablation and debris cover observations on Hinarche Glacier, *Mt. Res. Dev.*, *30*(2), 169–177.
Mihalcea, C., C. Mayer, G. Diolaiuti, C. D'Agata, C. Smiraglia, A. Lambrecht, E. Vuillermoz, and G. Tartari (2008), Spatial distribution of debris thickness and melting from remote-sensing and meteorological data, at debris-covered Baltoro glacier, Karakoram, Pakistan, *Ann. Glaciol.*, *48*(1), 49–57.
MRT (2011), MODIS Reprojection Tool (MRT) user's manual (Release 4.1), Land Processes DAAC USGS Earth Resources Observation and Science (EROS) Center, 69 pp.
Nakawo, M., and G. J. Young (1981), Field experiments to determine the effect of a debris layer on ablation of glacier ice, *Ann. Glaciol.*, *2*, 85–91.
Nakawo, M., and G. J. Young (1982), Estimate of glacier ablation under a debris layer from surface temperature and meteorological variables, *J. Glaciol.*, *28*(98), 29–34.
Nash, J. E., and I. V. Sutcliffe (1970), River flow forecasting through conceptual models part I—A discussion of principles, *J. Hydrol.*, *10*, 282–290.
Naz, B. S., C. D. Frans, G. K. C. Clarke, P. Burns, and D. P. Lettenmaier (2014), Modeling the effect of glacier recession on streamflow response using a coupled glacio-hydrological model, *Hydrol. Earth Syst. Sci.*, *18*, 787–802, doi:10.5194/hess-18-787-2014.
New, M. G., M. Hulme, and P. D. Jones (2000), Representing twentieth century space-time climate variability. part II: Development of 1901– 96 monthly grids of terrestrial surface climate, *J. Clim.*, *13*, 2217–2238.
Nicholson, L., and D. I. Benn (2006), Calculating ice melt beneath a debris layer using meteorological data, *J. Glaciol.*, *52*(178), 463–470.
Oerlemans, J., and B. K. Reichert (2000), Relating glacier mass balance to meteorological data by using a seasonal sensitivity characteristic, *J. Glaciol.*, *46*(152), 1–6.
Paterson, W. (1994), *The Physics of Glaciers*, 480 pp., Pergamon/Elsevier Press, Tarrytown, New York.
Pellicciotti, F., C. Buergi, W. W. Immerzeel, M. Konz, and A. B. Shrestha (2012), Challenges and uncertainties in hydrological modeling of remote HinduKush-Karakoram-Himalayan (HKH) basins: Suggestions for calibration strategies, *Mt. Res. Dev.*, *32*, 39–50.
Ragettli, S., F. Pellicciotti, R. Bordoy, and W. W. Immerzeel (2013), Sources of uncertainty in modeling the glaciohydrological response of a Karakoram watershed to climate change, *Water Resour. Res.*, *49*, 6048–6066, doi:10.1002/wrcr.20450.
Rana, B., M. Nakawo, Y. Fukushima, and Y. Ageta (1997), Application of conceptual precipitation runoff model (HYCYMODEL) in a debris covered glacierized basin in Langtang valley, Nepal Himalaya, *Ann. Galciol.*, *25*, 347–352.
Rankl, M., C. Kienholz, and M. Braun (2014), Glacier changes in the Karakoram region mapped by multimission satellite imagery, *Cryosphere*, *8*, 977–989.
Rees, G., and D. N. Collins (2006), Regional differences in response of flow in glacier fed Himalayan rivers to climate warming, *Hydrol. Processes*, *20*, 2157–2169.
Reid, T. D., M. Carenzo, F. Pellicciotti, and B. W. Brock (2012), Including debris cover effects in a distributed model of glacier ablation, *J. Geophys. Res.*, *117*, D18105, doi:10.1029/2012JD017795.
Sarıkaya, M. A., M. P. Bishop, J. F. Shroder, and G. Ali (2013), Remote-sensing assessment of glacier fluctuations in the Hindu Raj, Pakistan, *Int. J. Rem. Sens.*, *34*(11), 3968–3985.
Schaefli, B., B. Hingray, M. Niggli, and A. Musy (2005), A conceptual glacio-hydrological model for high mountainous catchments, *Hydrol. Earth Syst. Sci.*, *9*, 95–109.
Schaner, N., N. Voisin, B. Nijssen, and D. P. Lettenmaier (2012), The contribution of glacier melt to streamflow, *Environ. Res. Lett.*, *7*, 034029.
Sellers, P. J., D. A. Randall, G. J. Collatz, J. A. Berry, C. B. Field, D. A. Dazlich, C. Zhang, G. D. Collelo, and L. Bounoua (1996), A revised land surface parameterization (SiB2) for atmospheric GCMs, Part I: Model formulation, *J. Clim.*, *9*, 676–705.
Shrestha, M., L. Wang, T. Koike, Y. Xue, and Y. Hirabayashi (2010), Improving the snow physics of WEB-DHM and its point evaluation at the SnowMIP sites, *Hydrol. Earth Syst. Sci.*, *14*, 2577–2594, doi:10.5194/hess-14-2577-2010.
Shrestha, M., L. Wang, Y. Hirabayashi, and T. Koike (2012a), Simulation of forest snow processes at Fraser using a energy balance based snowmelt model (WEB-DHM-S), *Ann. J. Hydraul. Eng. (JSCE)*, *56*, I229–I234.
Shrestha, M., L. Wang, T. Koike, Y. Xue, and Y. Hirabayashi (2012b), Modeling the spatial distribution of snow cover in the Dudhkoshi region of Nepal Himalaya, *J. Hydrometeorol.*, *13*, 204–222, doi:10.1175/JHM-D-10-05027.1.
Shrestha, M., L. Wang, T. Koike, H. Tsutsui, Y. Xue, and Y. Hirabayashi (2014), Correcting basin-scale snowfall in a mountainous basin using a distributed snowmelt model and remote-sensing data, *Hydrol. Earth Syst. Sci.*, *18*, 747–761, doi:10.5194/hess-18-747-2014.
Sicart, J. E., R. Hock, P. Ribstein, M. Litt, and, E. Ramirez (2011), Analysis of seasonal variations in mass balance and meltwater discharge of the tropical Zongo Glacier by application of a distributed energy balance model, *J. Geophys. Res.*, *116*, D13105, doi:10.1029/2010JD015105.
Singh, P., and V. Singh (2001), *Snow and Glacier Hydrology*, 742 pp., Kluwer Acad., Dordrecht, Netherlands.
Soulis, E. D., K. Snelgrove, N. Kouwen, F. Seglenieks, and D. L. Verseghy (2000), Towards closing the vertical water balance in Canadian atmospheric models: Coupling of the land surface scheme CLASS with the distributed hydrological model WATFLOOD, *Atmos. Ocean*, *30*(1), 251–269.
Storck, P., and D. P. Lettenmaier (1999), Predicting the effect of a forest canopy on ground snow accumulation and ablation in maritime climates, in *Proc. 67th Western Snow Conference (Lake Tahoe, California)*, edited by C. Troendle and K. Elder, pp. 1–12.
Tahir, A. A., P. Chevallier, Y. Arnaud, L. Neppel, and B. Ahmad (2011a), Modeling snowmelt-runoff under climate scenarios in the Hunza River basin, Karakoram Range, Northern Pakistan, *J. Hydrol.*, *409*(1–2), 104–117.

Tahir, A. A., P. Chevallier, Y. Arnaud, and B. Ahmad (2011b), Snow cover dynamics and hydrological regime of the Hunza River basin, Karakoram Range, Northern Pakistan, *Hydrol. Earth Syst. Sci.*, *15*(7), 2275–2290.
van Genuchten, M. T. (1980), A closed-form equation for predicting the hydraulic conductivity of unsaturated soils, *Soil Sci. Soc. Am. J.*, *44*, 892–898.
Verdin, K., and J. Verdin (1999), A topological system for the delineation and codification of the Earth's river basins, *J. Hydrol.*, *218*, 1–12.
Verseghy, D. (2009), CLASS—The Canadian Land Surface Scheme (Version 3.4): Technical Documentation (Version 1.1).
Verseghy, D. L. (1991), CLASS—A Canadian land surface scheme for GCMs. I. Soil model, *Int. J. Climatol.*, *11*, 111–133.
Viviroli, D., H. H. Dürr, B. Messerli, M. Meybeck, and R. Weingartner (2007), Mountains of the world, water towers for humanity: Typology, mapping, and global significance, *Water Resour. Res.*, *43*, W07447, doi:10.1029/2006WR005653.
Wake, C. P. (1989), Glaciochemical investigations as a tool to determine the spatial variation of snow accumulation in the central Karakoram, Northern Pakistan, *Ann. Glaciol.*, *13*, 279–284.
Walter, M. T., E. S. Brooks, D. K. McCool, L. G. King, M. Molnau, and J. Boll (2005), Process-based snowmelt modeling: Does it require more input data than temperature-index modeling?, *J. Hydrol.*, *300*, 65–75.
Wang, F., L. Wang, T. Koike, H. Zhou, K. Yang, A. Wang, and W. Li (2011), Evaluation and application of a fine-resolution global data set in a semiarid mesoscale river basin with a distributed biosphere hydrological model, *J. Geophys. Res.*, *116*, D21108, doi:10.1029/2011JD015990.
Wang, L., T. Koike, K. Yang, T. Jackson, R. Bindlish, and D. Yang (2009a), Development of a distributed biosphere hydrological model and its evaluation with the Southern Great Plains Experiments (SGP97 and SGP99), *J. Geophys. Res.*, *114*, D08107, doi:10.1029/2008JD010800.
Wang, L., T. Koike, K. Yang, and P. Yeh (2009b), Assessment of a distributed biosphere hydrological model against streamflow and MODIS land surface temperature in the upper Tone River Basin, *J. Hydrol.*, *377*, 21–34.
Wang, X., H. Xie, and T. Liang (2008), Evaluation of MODIS snow cover and cloud mask and its application in northern Xinjiang, China, *Remote Sens. Environ.*, *112*, 1497–1513, doi:10.1016/j.rse.2007.05.016.
Wigmosta, M. S., L. W. Vail, and D. P. Lettenmaier (1994), A distributed hydrology-vegetation model for complex terrain, *Water Resour. Res.*, *30*, 1665–1679, doi:10.1029/94WR00436.
Winiger, M., M. Gumpert, and H. Yamout (2005), Karakoram-Hindukush-Western Himalaya: Assessing high-altitude water resources, *Hydrol. Processes*, *19*, 2329–2338.
Xue, Y., S. Sun, D. Kahan, and Y. Jiao (2003), The impact of parameterizations in snow physics and interface processes on the simulation of snow cover and runoff at several cold region sites, *J. Geophys. Res.*, *108*(D22), 8859, doi:10.1029/2002JD003174.
Yang, D., T. Koike, and H. Tanizawa (2004), Application of a distributed hydrological model and weather radar observation for flood management in the upper Tone River of Japan, *Hydrol. Processes*, *18*, doi:10.1002/hyp.5752.
Yang, Z.-L., R. E. Dickinson, A. Robock, and K. Y. Vinnikov (1997), Validation of snow submodel of the biosphere-atmosphere transfer scheme with Russian snow cover and meteorological observational data, *J. Clim.*, *10*, 48–66.
Yatagai, A., K. Kamiguchi, O. Arakawa, A. Hamada, N. Yasutomi, and A. Kitoh (2012), APHRODITE: Constructing a long-term daily gridded precipitation dataset for Asia based on a dense network of rain gauges, *Bull. Am. Meteorol. Soc.*, *93*, 1401–1415.
Young, G. J., and K. Hewitt (1990), Hydrology research in the upper Indus Basin, Karakoram Himalaya, Pakistan, Hydrol. Mountainous Areas, Czechoslovakia, 139–152.
Zhang, L., F. Su, D. Yang, Z. Hao, and K. Tong (2013), Discharge regime and simulation for the upstream of major rivers over Tibetan Plateau, *J. Geophys. Res. Atmos.*, *118*, 8500–8518, doi:10.1002/jgrd.50665.
Zhang, Y., K. Fujita, S. Liu, Q. Liu, and T. Nuimura (2011), Distribution of debris thickness and its effect on ice melt at Hailuogou glacier, southeastern Tibetan Plateau, using in situ surveys and ASTER imagery, *J. Glaciol.*, *57*(206), 1147–1157.
Zhao, Q., B. Ye, Y. Ding, S. Zhang, S. Yi, J. Wang, D. Shangguan, C. Zhao, and H. Han (2013), Coupling a glacier melt model to the Variable Infiltration Capacity (VIC) model for hydrological modeling in north-western China, *Environ. Earth Sci.*, *68*, 87–101.